Monthly Notices of the ROYAL ASTRONOMICAL SOCIETY

MNRAS **500,** 4989–5008 (2021) doi:10.1093/mnras/staa3514
Advance Access publication 2020 November 13

Revealing the relation between black hole growth and host-galaxy compactness among star-forming galaxies

Q. Ni [1,2]★ W. N. Brandt,[1,2,3] G. Yang [4,5]★ J. Leja,[1,6] C.-T. J. Chen [7] B. Luo,[8,9,10] J. Matharu [4,5] M. Sun,[11] F. Vito [12,13] Y. Q. Xue[14,15] and K. Zhang [16]

[1]*Department of Astronomy and Astrophysics, The Pennsylvania State University, 525 Davey Laboratory, University Park, PA 16802, USA*
[2]*Institute for Gravitation and the Cosmos, The Pennsylvania State University, University Park, PA 16802, USA*
[3]*Department of Physics, The Pennsylvania State University, 104 Davey Laboratory, University Park, PA 16802, USA*
[4]*Department of Physics and Astronomy, Texas A&M University, College Station, TX 77843-4242, USA*
[5]*George P. and Cynthia Woods Mitchell Institute for Fundamental Physics and Astronomy, Texas A&M University, College Station, TX 77843-4242, USA*
[6]*Center for Astrophysics | Harvard & Smithsonian, 60 Garden St, Cambridge, MA 02138, USA*
[7]*Marshall Space Flight Center, Huntsville, AL 35811, USA*
[8]*School of Astronomy and Space Science, Nanjing University, Nanjing 210093, China*
[9]*Key Laboratory of Modern Astronomy and Astrophysics, Nanjing University, Ministry of Education, Nanjing 210093, China*
[10]*Collaborative Innovation Center of Modern Astronomy and Space Exploration, Nanjing 210093, China*
[11]*Department of Astronomy, Xiamen University, Xiamen, Fujian 361005, China*
[12]*Instituto de Astrofísica and Centro de Astroingeniería, Facultad de Física, Pontificia Universidad Católica de Chile, Casilla 306, Santiago 22, Chile*
[13]*Chinese Academy of Sciences South America Center for Astronomy, National Astronomical Observatories, CAS, Beijing 100012, China*
[14]*CAS Key Laboratory for Research in Galaxies and Cosmology, Department of Astronomy, University of Science and Technology of China, Hefei 230026, China*
[15]*School of Astronomy and Space Science, University of Science and Technology of China, Hefei 230026, China*
[16]*Department of Astronomy, University of California, Berkeley, CA 94720-3411, USA*

Accepted 2020 November 9. Received 2020 November 3; in original form 2020 May 8

ABSTRACT

Recent studies show that a universal relation between black hole (BH) growth and stellar mass ($M_\star$) or star formation rate (SFR) is an oversimplification of BH–galaxy coevolution, and that morphological and structural properties of host galaxies must also be considered. Particularly, a possible connection between BH growth and host-galaxy compactness was identified among star-forming (SF) galaxies. Utilizing ≈6300 massive galaxies with $I_{814W} < 24$ at $z < 1.2$ in the Cosmic Evolution Survey (COSMOS) field, we perform systematic partial correlation analyses to investigate how sample-averaged BH accretion rate ($\overline{\mathrm{BHAR}}$) depends on host-galaxy compactness among SF galaxies, when controlling for morphology and $M_\star$ (or SFR). The projected central surface mass density within 1 kpc, Σ_1, is utilized to represent host-galaxy compactness in our study. We find that the $\overline{\mathrm{BHAR}}$–Σ_1 relation is stronger than either the $\overline{\mathrm{BHAR}}$–$M_\star$ or $\overline{\mathrm{BHAR}}$–SFR relation among SF galaxies, and this $\overline{\mathrm{BHAR}}$–Σ_1 relation applies to both bulge-dominated galaxies and galaxies that are not dominated by bulges. This $\overline{\mathrm{BHAR}}$–Σ_1 relation among SF galaxies suggests a link between BH growth and the central gas density of host galaxies on the kpc scale, which may further imply a common origin of the gas in the vicinity of the BH and in the central ∼kpc of the galaxy. This $\overline{\mathrm{BHAR}}$–Σ_1 relation can also be interpreted as the relation between BH growth and the central velocity dispersion of host galaxies at a given gas content (i.e. gas mass fraction), indicating the role of the host-galaxy potential well in regulating accretion on to the BH.

Key words: galaxies: active – galaxies: evolution – galaxies: nuclei – X-rays: galaxies .

1 INTRODUCTION

Correlations between black hole (BH) mass and host-galaxy properties observed in the local Universe (e.g. Magorrian et al. 1998; Marconi & Hunt 2003; Kormendy & Ho 2013; McConnell & Ma 2013) have inspired investigations of so-called 'BH–galaxy coevolution' over the past couple decades. As the BH accretion rate of individual objects has large long-term variability that hinders us from revealing any intrinsic link between the BH growth and its host galaxy (e.g. Hickox et al. 2014; Sartori et al. 2018; Yuan et al. 2018), one effective way to investigate BH–galaxy coevolution 'in action' is performing large-sample studies. With X-ray emission serving as a reliable tracer of BH accretion (e.g. Brandt & Alexander 2015), these sample studies utilize the average BH accretion rate ($\overline{\mathrm{BHAR}}$) of a sample of galaxies sharing similar properties to approximate the long-term average BH growth of galaxies with these properties, i.e. they take BH growth to be ergodic. Relations between $\overline{\mathrm{BHAR}}$ and stellar mass ($M_\star$) or star formation rate (SFR) have been revealed (e.g. Mullaney et al. 2012; Chen et al. 2013; Aird, Coil & Georgakakis 2017, 2018; Yang et al. 2017, 2018a), which are considered as observational evidence of a link

★ E-mail: qxn1@psu.edu (QN); gyang206265@gmail.com (GY)

between BH growth and the potential well or the gas mass of host galaxies.

However, a 'universal' relation between BH growth and $M_\star$ or SFR is likely a substantial oversimplification of BH–galaxy coevolution. Yang et al. (2019) found that morphology must be considered when studying BH–galaxy coevolution: for bulge-dominated (BD) galaxies, BH growth mainly depends on SFR rather than $M_\star$; for galaxies not dominated by bulges (non-BD), BH growth mainly depends on $M_\star$ rather than SFR. This finding is consistent with the observational result in the local Universe that BH mass ($M_{\rm BH}$) only correlates tightly with bulge mass ($M_{\rm bulge}$), rather than $M_\star$ of the whole host galaxy (e.g. Kormendy & Ho 2013). The role of compactness (which measures the mass-to-size ratio of galaxies) has also triggered attention in recent years: Kocevski et al. (2017) found an elevated active galactic nucleus (AGN) fraction among compact star-forming (SF) galaxies when compared with mass-matched extended SF galaxies. This finding is consistent with the predicted scenario that BH growth can be triggered by the high central gas density during a wet compaction event (e.g. Wellons et al. 2015; Dekel, Lapiner & Dubois 2019; Habouzit et al. 2019).

Given all these findings, Ni et al. (2019) examined the effectiveness of compactness in predicting the amount of BH growth when controlling for various other host-galaxy properties (including morphology) using galaxies in the $\approx$0.25 deg^2 Cosmic Assembly Near-infrared Deep Extragalactic Legacy Survey (CANDELS) fields (Grogin et al. 2011; Koekemoer et al. 2011). Ni et al. (2019) found that compactness can only effectively predict $\overline{\rm BHAR}$ among SF galaxies, and the central surface mass density within 1 kpc (Σ_1) is more effective in predicting the amount of BH growth than the surface mass density in the central regions comprising 50 per cent of the galaxy stellar mass. These results led Ni et al. (2019) to speculate that the $\overline{\rm BHAR}$–Σ_1 relation, if confirmed, could reflect a link between BH growth and the central $\sim$kpc gas density of host galaxies (that could be related to Σ_1 among SF galaxies when assuming a correlation between gas density and $M_\star$ density, which is supported by the recent Atacama Large Millimeter/submillimeter Array (ALMA) observational results; see Lin et al. 2019). Ni et al. (2019) found evidence that the relation between $\overline{\rm BHAR}$ and Σ_1 is not simply a secondary manifestation of the $\overline{\rm BHAR}$–$M_\star$ relation among SF non-BD galaxies; while the number of SF BD galaxies in Ni et al. (2019) was too small to confirm a significant ($>3\sigma$) $\overline{\rm BHAR}$–Σ_1 relation (when controlling for SFR), BD galaxies with relatively high SFR values suggest the link between BH growth and Σ_1. If a significant $\overline{\rm BHAR}$–Σ_1 relation can be confirmed among SF BD galaxies (when controlling for SFR), it will provide a natural explanation for overmassive BH 'monsters'[1] in the local Universe that live in compact galaxies (e.g. Kormendy & Ho 2013; Walsh et al. 2015, 2017). It is plausible that a $\overline{\rm BHAR}$–Σ_1 relation that is more 'fundamental'[2] than either the $\overline{\rm BHAR}$–$M_\star$ or $\overline{\rm BHAR}$–SFR relation may apply for *all* SF galaxies regardless of morphology. If so, this would provide strong evidence for a link between BH growth and the central gas density of host galaxies, which may reveal how BHs feed from gas in the central parts of galaxies: this is especially important given that it is difficult to measure the central gas density directly for a large sample of AGNs due to current observational constraints.

In this paper, we use a large sample of galaxies and AGNs at $z < 1.2$ in the $\approx$1.4 deg^2 Cosmic Evolution Survey (COSMOS) field (which has the UltraVISTA and Advanced Camera for Surveys (ACS) coverage; Koekemoer et al. 2007; Leauthaud et al. 2007; Laigle et al. 2016) to probe further the relation between BH growth and host-galaxy compactness among SF galaxies. Specifically, we will address the following questions: Is the $\overline{\rm BHAR}$–Σ_1 relation more fundamental than the $\overline{\rm BHAR}$–$M_\star$ relation among SF non-BD galaxies? Is there a significant $\overline{\rm BHAR}$–Σ_1 relation when controlling for SFR among SF BD galaxies? Is the $\overline{\rm BHAR}$–Σ_1 relation 'universal' among all SF galaxies? If so, what are the properties of this $\overline{\rm BHAR}$–Σ_1 relation?

This paper is structured as follows. In Section 2, we describe the sample construction process. In Section 3, we perform data analyses and present the results. In Section 4, we interpret the analyses results and present relevant discussions. Section 5 summarizes this work and discusses future prospects. Throughout this paper, $M_\star$ is in units of $\rm M_\odot$; SFR and $\overline{\rm BHAR}$ are in units of $\rm M_\odot\ yr^{-1}$; Σ_1 is in units of $\rm M_\odot/kpc^2$. $L_{\rm X}$ indicates absorption-corrected X-ray luminosity at rest frame 2–10 keV in units of erg s^{-1}. Quoted uncertainties are at the 1σ (68 per cent) confidence level, unless otherwise stated. A cosmology with $H_0 = 70$ km s^{-1} Mpc^{-1}, $\Omega_{\rm M} = 0.3$, and $\Omega_\Lambda = 0.7$ is assumed. We consider a partial correlation (PCOR) to be significant if it has a p-value < 0.0027, which corresponds to a significance level $>3\sigma$. Significant results throughout the paper are marked in bold in the tables.

2 DATA AND SAMPLE

Our objects are selected from the COSMOS2015 catalogue (Laigle et al. 2016). Only sources within both the COSMOS and UltraVISTA regions are kept, and we remove saturated objects in bad areas (FLAG_COSMOS = 0, FLAG_HJMCC = 0, and FLAG_PETER = 0). We further limit our selection to $I_{\rm F814W} < 24$ galaxies: $I_{\rm F814W} < 24$ is a common threshold adopted in the *Hubble Space Telescope* (*HST*) COSMOS field for morphological classifications (e.g. Scarlata et al. 2007). We obtain spectroscopic redshifts (spec-z) for sources from Marchesi et al. (2016a), Delvecchio et al. (2017), Hasinger et al. (2018), and Salvato et al. (in preparation). We note that $\approx$60 per cent of sources utilized in Section 3 have spectroscopic redshifts. For sources without spectroscopic redshifts, we adopt the high-quality photometric redshift (photo-z) measurements from Laigle et al. (2016) with $\sigma_{\Delta z/(1+z_{\rm s})} = 0.007$.

For the selected COSMOS sources, in Section 2.1, we measure their $M_\star$ and SFR values; in Section 2.2, we measure their structural parameters including Sérsic index (n) and effective radius ($r_{\rm e}$) that will be utilized to calculate Σ_1; and in Section 2.3, we classify objects as BD/non-BD. In Section 2.4, we construct samples that will be used for the analyses in Section 3. In Section 2.5, we explain how $\overline{\rm BHAR}$ utilized in Section 3 is estimated.

2.1 Stellar mass and star formation rate measurements

We measure $M_\star$ and SFR with X-CIGALE (Yang et al. 2020), which is a new version of CIGALE (e.g. Boquien et al. 2019) with updated AGN modules. Photometric data in 38 bands (including 24 broad-bands) from near-ultraviolet (NUV) to far-infrared (FIR; Laigle et al. 2016) are utilized. For the NUV to near-infrared (NIR) photometry, we correct the aperture flux to total flux following appendix A2 of

[1]BH 'monsters' are BHs that have $M_{\rm BH}$ significantly larger than expected from the $M_{\rm BH}$ relation with bulge mass ($M_{\rm bulge}$). We note that it has also been argued that some BH monsters are not real: their BH masses seem to be unexpectedly large due to the underestimation of $M_{\rm bulge}$ when improper bulge/disc decomposition is conducted (e.g. Graham et al. 2016).

[2]Throughout this paper, when A relates with both B and C, if the relation between A and B is significant when controlling for C while the relation between A and C is not significant when controlling for B in partial correlation (PCOR) analyses, we say the relation between A and B is more fundamental than the relation between A and C.

Laigle et al. (2016). For the three *Herschel*/Spectral and Photometric Imaging Receiver (SPIRE) bands, we use photometric data reported in a superdeblended catalogue described in Jin et al. (2018) that utilizes the deblending technique in Liu et al. (2018).

For X-ray undetected galaxies, we fit them with a two-run approach: we first fit them with pure galaxy templates. We adopt a delayed exponentially declining star formation history (SFH),[3] a Chabrier initial mass function (Chabrier 2003), the extinction law from Calzetti et al. (2000), and the dust emission template from Dale et al. (2014), following Ciesla et al. (2015) and Yang et al. (2020). We also add nebular emission to the SED libraries. Details of the fitting parameters can be seen in Table A1. Then, we add an additional AGN component presented in X-CIGALE, SKIRTOR (that is established based on Stalevski et al. 2012, 2016), during the fitting (detailed parameters can also be found in Table A1). One free parameter in SKIRTOR is the fractional contribution of AGN emission to the total infrared (IR) luminosity ($\mathrm{frac_{AGN}}$), which can range from 0 to 1, and we use a step of 0.1 during the fitting. We find that while the measurements of $M_\star$ are not significantly influenced by adding an AGN component, the SFR measurements are smaller by ≈0.2–0.5 dex on average when $\mathrm{frac_{AGN}} \geqslant 0.3$. When $\mathrm{frac_{AGN}} < 0.3$, adding an AGN component affects the SFR measurements by less than ≈0.2 dex. As we group sources in log SFR bins of at least ∼0.5 dex width in our analyses (see Section 3.2), the differences in SFR measurements caused by adding an AGN component for $\mathrm{frac_{AGN}} < 0.3$ objects are negligible in the context of this work. Thus, when the estimated Bayesian 1σ lower limit of $\mathrm{frac_{AGN}}$ is $\geq$0.25 (≈1 per cent of total objects), we adopt the Bayesian $M_\star$ and SFR values from the solution with an AGN component. Otherwise, we adopt the Bayesian $M_\star$ and SFR values from the solution without an AGN component.

For X-ray detected galaxies, we directly fit them with both galaxy and AGN components. We have also incorporated the *Chandra* X-ray flux (Civano et al. 2016) into the fitting following Yang et al. (2020) (through the X-ray module in X-CIGALE) to constrain the AGN SED contribution, as the X-ray SED of AGN is empirically connected to the UV-to-IR SED (e.g. Just et al. 2007). *Chandra* X-ray fluxes are adopted following the preference order of hard band (2–10 keV), full band (0.5–10 keV), and soft band (0.5–2 keV), thus minimizing the effects of X-ray obscuration. We require that the deviation from this empirical SED relation ($\Delta\alpha_{\mathrm{OX}}$) is not larger than 0.2 (which corresponds to the 2σ scatter of the empirical relation; e.g. Just et al. 2007). We note that for our X-ray detected galaxies, adding the X-ray module or not does not significantly affect the Bayesian $M_\star$ and SFR measurements: the scatter between the two sets of $M_\star$ (SFR) measurements is ≈0.1 (0.2) dex, with negligible systematic offsets. We verified that the analysis results in Section 3 do not change qualitatively if we add random perturbations to $\log M_\star$/log SFR values of X-ray detected galaxies with a scatter of 0.1/0.2 dex.

A comparison between our SED-based $M_\star$ and SFR measurements and SED-based $M_\star$ and SFR measurements with PROSPECTOR (Leja et al. 2020) for a subset of COSMOS galaxies is presented in Appendix A, showing the general consistency between the two approaches. As our $M_\star$ measurements are systematically smaller than those reported in Leja et al. (2020) by ≈0.15 dex, we correct our measurements for this systematic offset in the final adopted $M_\star$ values (see Appendix A for details).

[3]The delayed SFH is chosen as Ciesla et al. (2015) found that when performing spectral energy distribution (SED) fitting with CIGALE for AGN hosts, the delayed SFH model provides better estimation of $M_\star$ and SFR compared with other parametric SFHs.

As the SED fitting process is 'dominated' by the large number of UV-to-NIR bands that may underestimate SFR in the high-SFR regime (e.g. Wuyts et al. 2011; Yang et al. 2017), FIR-based SFR values are adopted when available (for ≈4 per cent/26 per cent of objects in the SF BD/SF non-BD samples defined in Section 2.4). When an object is detected with signal-to-noise ratio (S/N) > 5 in a *Herschel* band (Lutz et al. 2011; Oliver et al. 2012; Laigle et al. 2016; Jin et al. 2018), we derive its total IR luminosity from the FIR flux in this band utilizing the SF galaxy template in Kirkpatrick et al. (2012). Then, a weighted total IR luminosity is calculated from all available *Herschel* bands with the FIR flux error serving as the weight. The total IR luminosity is then converted to SFR following equation (1) in Ni et al. (2019), assuming that most UV photons are absorbed by the dust. We have also compared our SED-based SFR values with these FIR-based SFR values, showing the consistency of these two methods (see Appendix A for details). We note that FIR-based SFR measurement also has its shortcomings (e.g. Kennicutt 1998a; Hodge & da Cunha 2020): as the stellar populations and dust properties vary from galaxy to galaxy, there are natural uncertainties associated with the simple universal rescaling from FIR luminosity to SFR. We verified that our results in Section 3 do not change qualitatively if we solely adopt SED-based SFR values.

2.2 Structural measurements with GALFIT

2.2.1 Image and noise cut-outs

We prepare image cut-outs for the selected objects from ACS F814W COSMOS science images v2.0 (Koekemoer et al. 2007) that have bad pixels and cosmic rays removed. Following Matharu et al. (2019), our cut-outs have 15 × FLUX_RADIUS pixels in the *x*/*y*-axis (FLUX_RADIUS is the half-light radius measured by SExtractor in Leauthaud et al. 2007), with the target galaxy at the centre. The noise cut-outs with same sizes are made following van der Wel et al. (2012) and Matharu et al. (2019), where the noise is a quadrature combination of the Poisson noise of the image and other noises where the sky-background noise dominates. We estimate the sky-background noise and the background sky level with segmentation maps generated for each image cut-out by SExtractor v2.19.5 (Bertin & Arnouts 1996), following section 3 and table 1 of Leauthaud et al. (2007). With the information provided by these segmentation maps, we select all pixels that do not belong to sources in the image cut-out, and use these pixels to estimate the background sky level/noise, which is the mean/root-mean-square value of these background pixels.

2.2.2 PSF generation

The point spread function (PSF) model used in this work is generated by the IDL wrapper of TinyTim (Krist 1995) introduced in Rhodes et al. (2006, 2007), assuming a G8V star and a focus at −3.0 μm. This IDL wrapper can generate the PSF model with a pixel scale of 0.03 arcsec to match the oversampled version of ACS COSMOS science images that have geometric distortion removed. We neglect the change of PSF both temporally and across the CCD at the level of a few per cent (Rhodes et al. 2007; Gabor et al. 2009). We have also compared the PSF model with real stars in the COSMOS field, and we find that the differences between the encircled flux fractions at a given radius are generally small (within a few per cent).

2.2.3 GALFIT set-up

We fit our objects with a single-component Sérsic profile in GALFIT (Peng et al. 2002):

$$I(r) = I_{\rm o} \exp\left\{-b_n\left[\left(\frac{r}{r_{\rm e}}\right)^{1/n} - 1\right]\right\}, \quad (1)$$

where n is the Sérsic index, $r_{\rm e}$ is the half-light radius, $I(r)$ represents light intensity at a radius of r, $I_{\rm o}$ is the light intensity at $r_{\rm e}$, and b_n is coupled to n to make half of the total flux lie within $r_{\rm e}$.

Following van der Wel et al. (2012), we set constraints in GALFIT to keep $0.2 < n < 8$, $0.5 < r_{\rm e} < 800$ (in units of pixels), and $0.0001 < q < 1$ (q is the axial ratio). Rather than fitting a single object, we fit all the sources in the cut-out that are no more than 5 mag fainter than the central target source simultaneously, which can substantially improve the accuracy of fitting (e.g. Peng et al. 2002; Matharu et al. 2019). We do not fit for the sky during the fit (e.g. Häussler et al. 2007; Barden et al. 2012): we set the sky level as the background sky level estimated in Section 2.2.1. For ≈87 per cent of objects, GALFIT reached a solution without hitting any constraints (we mark them with GALFIT_FLAG = 0); for ≈4 per cent of objects, GALFIT hit the constraints (we mark them with GALFIT_FLAG = 2); for ≈9 per cent of objects, GALFIT did not manage to converge. Since fitting a large number of additional objects simultaneously may cause GALFIT to fail due to these objects, we fit the ≈9 per cent of objects where GALFIT did not manage to converge again without fitting neighbouring objects: in this second run, we use the SExtractor segmentation map to mask all neighbouring objects (masked pixels within an ellipse of 3 × Kron ellipse + 20 pixels of the central object are regarded to contain the source flux, so we unmask them in the segmentation map), and we only fit the target object at the centre. If GALFIT reached a solution without hitting any constraints in this second run, we mark the object with GALFIT_FLAG = 1; if GALFIT hit the constraints, we mark the object with GALFIT_FLAG = 2; if GALFIT failed again, we mark the object with GALFIT_FLAG = 3. We will only use the ≈87 per cent GALFIT_FLAG = 0 and ≈8 per cent GALFIT_FLAG = 1 object for our analyses, and our results do not change qualitatively if we limit our analyses to GALFIT_FLAG = 0 objects only. In Appendix B, we show the reliability of our results by comparing with the GIM2D measurements of $I_{\rm F814W} < 22.5$ galaxies in COSMOS (Sargent et al. 2007). We also assess the level of potential AGN contamination to host-galaxy light profiles in Appendix B. We find that for X-ray AGNs included in our sample (see Section 2.4 for the sample selection), the AGN contamination is largely negligible.

2.3 Deep-learning-based morphology

We use a deep-learning-based method to classify $I_{\rm F814W} < 24$ galaxies in COSMOS (Leauthaud et al. 2007) as BD galaxies or non-BD galaxies. Details of this deep-learning-based BD/non-BD classification process are presented in Appendix C. Our selection of BD galaxies is broadly consistent with the selection of 'pure bulges' in Huertas-Company et al. (2015, see Appendix C for details).

2.4 Sample construction

We first confine our sample to galaxies at $z < 1.2$, where the *HST* F814W band can characterize the rest-frame optical emission of galaxies (≈370–800 nm), so that our morphological measurements are not strongly affected by the 'morphological k-correction'. The relatively low redshift range probed here compared with the $z = 0.5$–3 sample in Ni et al. (2019) also generally enables more accurate more accurate morphological characterization. Following Yang et al. (2018a) and Ni et al. (2019), we remove broad-line (BL) AGNs (Marchesi et al. 2016a) from the sample (which make up ≈6 per cent of total X-ray detected galaxies), as the strong emission from BL AGNs prohibits us from obtaining reliable measurements of host-galaxy properties. The exclusion of BL AGNs should not affect the analysis results assuming the unified model (e.g. Netzer 2015). According to the unified model, BL AGNs and type 2 AGNs are purely orientation-based AGN classes: when our line of sight does not intercept the torus, a BL AGN is observed; otherwise, a type 2 AGN is observed. Thus, as detailed in section 2.4.1 of Ni et al. (2019), excluding the contribution from BL AGNs when estimating sample-averaged BH growth only decreases $\overline{\rm BHAR}$ by a similar fraction for utilized subsamples of galaxies in Section 3, so it will not influence our investigations of the dependence of BH growth on various host-galaxy properties.[4] We also confine our sample to GALFIT_FLAG = 0 or 1 object, where reliable structural measurements are available (see Section 2.2). Through doing this, we also reject AGNs that cause strong contamination to the host-galaxy light profiles as we do not take objects with extremely large n. In this step, an additional ≈10 per cent of X-ray detected galaxies are removed. We calculate Σ_1 values for the selected galaxies assuming a constant $M_\star$-to-light ratio throughout the galaxy, with $M_\star$ measured in Section 2.1, and $I(r)$ measured in Section 2.2:

$$\Sigma_1 = \frac{\int_0^{1\,\rm kpc} I(r) 2\pi r\,{\rm d}r}{\int_0^{\infty} I(r) 2\pi r\,{\rm d}r} \frac{M_\star}{\pi(1\,\rm kpc)^2}. \quad (2)$$

When assuming a constant $M_\star$-to-light ratio throughout the galaxy, we are actually assuming a rather homogeneous stellar population constitution across the whole galaxy. As discussed in Whitaker et al. (2017) and references therein, $M_\star$ profiles typically follow the rest-frame optical light profiles well, though they are more centrally concentrated in general. Thus, Σ_1 may be underestimated when we use equation (2) to perform the extrapolation. We have compared the Σ_1 values in Ni et al. (2019) (which are also measured utilizing equation (2), but for the CANDELS fields) with the Σ_1 values reported in Barro et al. (2017) that are derived from spatially resolved SED fitting with multiband *HST* light profiles. The extrapolated Σ_1 values of SF galaxies (which are the objects of study in this work) are systematically smaller by ≈0.15 dex than the Σ_1 values measured in Barro et al. (2017), with a scatter of ≈0.3 dex. When we limit the comparison to X-ray detected galaxies, the offset and scatter are similar. We also note that the offset and scatter do not vary significantly with SFR or $L_{\rm X}$ among SF galaxies. This indicates that our assumption of a constant $M_\star$-to-light ratio roughly holds.

We use the star formation main sequence derived in Whitaker et al. (2012) at the appropriate redshift to select SF galaxies: if the SFR value of a galaxy is above the star formation main sequence or

[4]We recognize that it has been suggested that host-galaxy gas could have column densities on the order of 10^{23-24} cm^{-2} for $z > 3$ compact SF galaxies (D'Amato et al. 2020), indicating that the unified model may not be sufficient for explaining all obscured AGNs. However, as our study focuses on low-to-moderate-redshift galaxies, the gas content is not as high as that of high-z galaxies. Buchner & Bauer (2017) suggest that at $z < 3$, galaxy-scale gas does not generally produce Compton-thick columns. This is consistent with our checking that when we group X-ray AGNs in our sample into several Σ_1 bins, the average X-ray hardness ratio does not significantly vary: if the galaxy-scale gas column density among compact SF galaxies in our sample is sufficiently large, we would expect harder X-ray spectra in average among AGNs hosted by more compact SF galaxies. Thus, the unified model appears to be a reliable assumption to first order for our work.

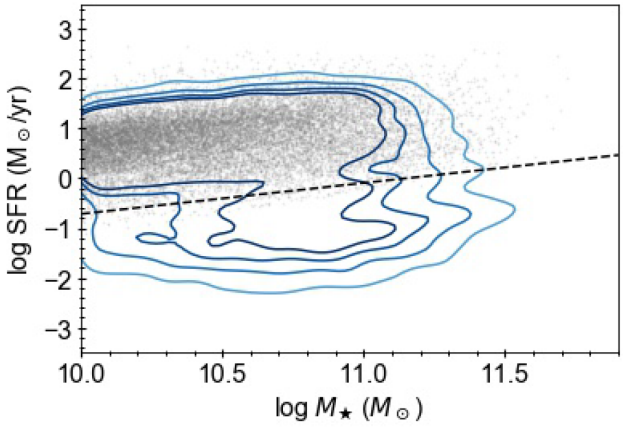

Figure 1. Selected SF galaxies (grey dots) in the SFR versus $M_\star$ plane. The contours encircle 68 per cent, 80 per cent, 90 per cent, and 95 per cent of $I_{814W} < 24$ massive ($\log M_\star > 10$) galaxies at $z < 1.2$ in the COSMOS field. The black dashed line shows the division between SF galaxies and quiescent galaxies at $z = 0.6$.

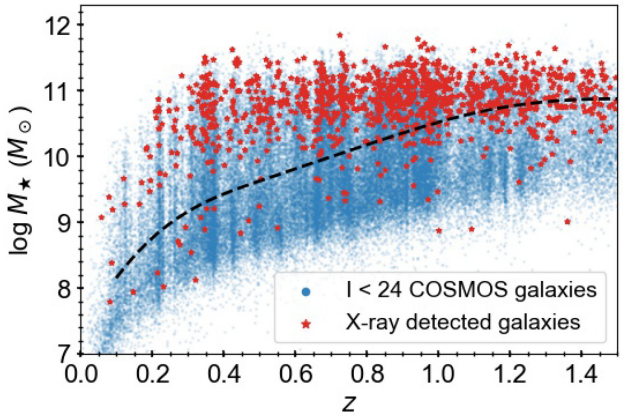

Figure 2. $M_\star$ as a function of redshift. The background blue dots depict all $I_{814W} < 24$ galaxies in the COSMOS field. The red stars represent X-ray detected sources. The dashed curve indicates the $M_\star$ completeness limit as a function of redshift.

no more than 1.4 dex below the star formation main sequence, we classify this galaxy as a SF galaxy. This division roughly corresponds to galaxies lying above the local minimum in the distribution of SFRs at a given $M_\star$ (see Fig. 1).

We construct a SF non-BD sample and a SF BD sample to study the role of Σ_1 in predicting BH growth when controlling for morphology and $M_\star$ (or SFR). The SF non-BD sample will be used in Section 3.1 to assess if the $\overline{\rm BHAR}$–Σ_1 relation is more fundamental than the $\overline{\rm BHAR}$–$M_\star$ relation. As the relation between $\overline{\rm BHAR}$ and $M_\star$ or Σ_1 has cosmic evolution (e.g. Mullaney et al. 2012; Yang et al. 2018a; Ni et al. 2019), we require that the SF non-BD sample is mass complete and has a uniform mass cut across the entire probed redshift range, so that the probed relation will not be significantly affected by the cosmic evolution. The $M_\star$ completeness curve as a function of redshift for $I_{F814W} < 24$ COSMOS galaxies is shown in Fig. 2. The limiting $M_\star$ is derived following section 3.2 of Ilbert et al. (2013) and section 2.4.1 of Ni et al. (2019). By selecting $\log M_\star > 10.2$ SF non-BD galaxies at $z < 0.8$ ($\log M_\star = 10.2$ is the limiting $M_\star$ at $z = 0.8$), we constitute the SF non-BD sample with a sample size of ≈6000, six times that in Ni et al. (2019) in similar $M_\star$ and z ranges. We note that ≈78 per cent of total non-BD galaxies in the same $M_\star$ and z ranges are SF non-BD galaxies. Thus, studying the relations between BH growth and various host-galaxy properties in the SF non-BD sample can help us investigate BH–galaxy coevolution in the majority of the non-BD population.

The SF BD sample will be used in Section 3.2 to test if the $\overline{\rm BHAR}$–Σ_1 relation exists when controlling for SFR. According to Yang et al. (2019), $\overline{\rm BHAR}$ among BD galaxies follows a linear relation with SFR in the log–log space with no obvious additional dependence on $M_\star$, and no evident cosmic evolution is found for this relation. Thus, a mass-complete sample of SF BD galaxies or a sample in a narrow redshift bin is not necessary to test if the conclusion of Yang et al. (2019) holds true, or if Σ_1 is indeed playing an important role in predicting the amount of BH growth in this subpopulation. Therefore, we select all massive ($\log M_\star > 10$) SF BD galaxies at $z < 1.2$ to constitute the SF BD sample, which gives us a large sample of ≈1000 galaxies, three times that in Ni et al. (2019) in the similar redshift range. We note that while galaxies in the SF BD sample only make up ≈20 per cent of total BD galaxies in the same $M_\star$ and z ranges, ≈76 per cent of the BH growth takes place within these ≈20 per cent of objects (we estimate the amount of BH growth as described in Section 2.5), which makes characterizing the relation between BH growth and host-galaxy properties particularly important for this subsample.

The properties of the SF non-BD sample and the SF BD sample are shown in Table 1. In Fig. 3, we show the Σ_1 versus $M_\star$ and Σ_1 versus SFR distributions for the SF non-BD sample and the SF BD sample, demonstrating the parameter space probed in this work.

We also construct a sample of SF galaxies to study the properties of the $\overline{\rm BHAR}$–Σ_1 relation regardless of morphology in Section 3.3. This sample (we call it the ALL SF sample in short hereafter) is a mass-complete sample with a sample size of ≈6300, constituted by all SF galaxies with $\log M_\star > 10.2$ at $z < 0.8$. The properties of the ALL SF sample are also listed in Table 1.

2.5 Sample-averaged black hole accretion rate

Following Yang et al. (2018b) and Ni et al. (2019), we calculate $\overline{\rm BHAR}$ for a given sample of galaxies sharing similar properties with contributions from both X-ray detected sources and X-ray undetected sources to cover all BH accretion, thereby estimating the *long-term average BH growth* (see Section 1).

The X-ray fluxes of detected sources are adopted from the COSMOS-Legacy X-ray survey catalogue (Civano et al. 2016), which is obtained from deep *Chandra* observations in the field. We convert the X-ray fluxes (following the preference order of hard band, full band, and soft band, thus minimizing the effects of X-ray obscuration) to L_X assuming a power-law model with Galactic absorption and $\Gamma = 1.7$ (e.g. Marchesi et al. 2016b; Yang et al. 2016). As discussed in Yang et al. (2018b), the underestimation of X-ray flux due to obscuration in this scheme is small on average (≈20 per cent). We account for this systematic effect of obscuration by increasing the X-ray fluxes of detected sources by 20 per cent, following Yang et al. (2019) and Ni et al. (2019). The X-ray emission of a group of X-ray undetected sources is taken into account via X-ray stacking techniques using the full-band *Chandra* X-ray image. Details of this stacking process can be seen in section 2.4.2 of Yang et al. (2018b).

Following section 2.3 of Ni et al. (2019), the average AGN bolometric luminosity ($\overline{L_{\rm bol}}$) for a given sample can be calculated

Table 1. Summary of sample properties. Column (1): name of the sample; column (2): redshift range of the sample; column (3): $M_\star$ range of the sample; column (4): number of galaxies in the sample; column (5): number of spec-z/photo-z sources; column (6): number of X-ray detected galaxies.

Sample name (1)	Redshift range (2)	Mass range (3)	Number of galaxies (4)	Number of spec-z/photo-z (5)	Number of X-ray detections (6)
SF non-BD	0–0.8	$\log M_\star > 10.2$	5979	3823/2156	179
SF BD	0–1.2	$\log M_\star > 10$	1020	421/599	81
ALL SF	0–0.8	$\log M_\star > 10.2$	6334	4041/2293	206

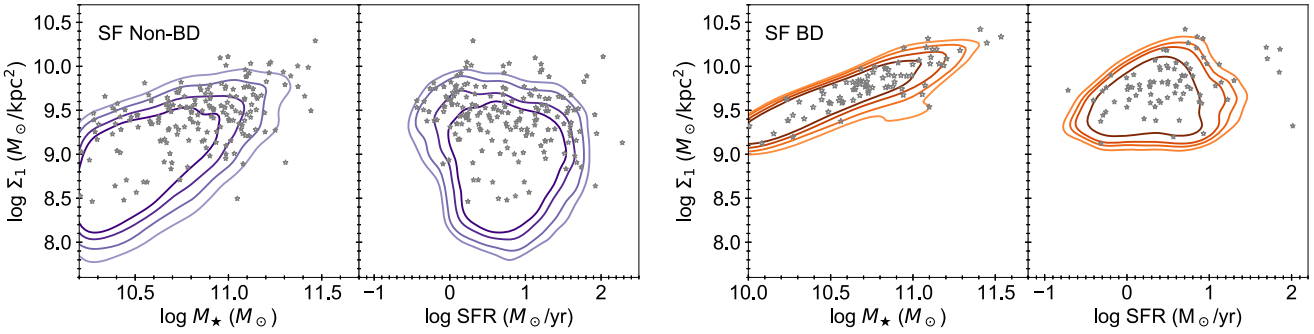

Figure 3. Left-hand panel: Σ_1 versus $M_\star$ and Σ_1 versus SFR for galaxies in the SF non-BD sample. The contours encircle 68 per cent, 80 per cent, 90 per cent, and 95 per cent of galaxies. The silver stars represent X-ray detected galaxies. Right-hand panel: similar to the left-hand panel, but for galaxies in the SF BD sample.

from $L_{\rm X}$ of each X-ray detected source and the average X-ray luminosity of all the X-ray undetected sources ($\overline{L_{\rm X,stack}}$) obtained via stacking, assuming the $L_{\rm X}$-dependent bolometric correction from Hopkins, Richards & Hernquist (2007). We also subtract the contributions from X-ray binaries (XRBs) from $L_{\rm X}$ and $\overline{L_{\rm X,stack}}$ before applying the bolometric correction. The XRB luminosity ($L_{\rm X,\,XRB}$) can be estimated through a redshift-dependent function of $M_\star$ and SFR (model 269, Fragos et al. 2013), which is derived utilizing observations in Lehmer et al. (2016).[5] The equation for calculating $\overline{L_{\rm bol}}$ is

$$\overline{L_{\rm bol}} = \frac{\left[\sum_{n=0}^{N_{\rm det}}(L_{\rm X}-L_{\rm X,XRB})k_{\rm bol}\right] + (\overline{L_{\rm X,stack}} - \overline{L_{\rm X,XRB}})N_{\rm non}\overline{k_{\rm bol}}}{N_{\rm det}+N_{\rm non}}, \quad (3)$$

where $N_{\rm det}$ ($N_{\rm non}$) represents the number of X-ray detected (undetected) galaxies; $L_{\rm X,\,XRB}$ ($\overline{L_{\rm X,XRB}}$) is the expected XRB luminosity in each individual X-ray detected galaxy (the average XRB luminosity expected for all X-ray undetected galaxies); $k_{\rm bol}$ ($\overline{k_{\rm bol}}$) is the $L_{\rm X}$-dependent bolometric correction applied to each individual X-ray detected galaxy (all X-ray undetected galaxies) calculated from $L_{\rm X}$ − $L_{\rm X,\,XRB}$ for this object ($\overline{L_{\rm X,stack}} - \overline{L_{\rm X,XRB}}$ of all X-ray undetected galaxies). In this equation, X-ray detected sources contribute most of the numerator (i.e. the total $L_{\rm bol}$ of the sample); X-ray undetected sources mainly contribute to the denominator by $N_{\rm non}$ (assuming ergodic BH growth, averaging the total $L_{\rm bol}$ over the whole sample is equivalent to averaging the total $L_{\rm bol}$ over the whole duty cycle). Then, $\overline{L_{\rm bol}}$ can be converted to $\overline{\rm BHAR}$ adopting a constant radiative efficiency of 0.1:[6]

$$\overline{\rm BHAR} = \frac{(1-\epsilon)\overline{L_{\rm bol}}}{\epsilon c^2} = \frac{1.58\overline{L_{\rm bol}}}{10^{46}\,{\rm erg\,s^{-1}}}\,{\rm M_\odot\,yr^{-1}}. \quad (4)$$

The uncertainty of $\overline{\rm BHAR}$ can be obtained via bootstrapping the sample (i.e. randomly drawing the same number of objects from the sample with replacement) 1000 times. For each bootstrapped sample, $\overline{\rm BHAR}$ is calculated, and the 16th and 84th percentiles of the obtained $\overline{\rm BHAR}$ distribution give the estimation of the 1σ uncertainty associated with $\overline{\rm BHAR}$ of the sample.

3 ANALYSES AND RESULTS

In Section 3.1, we will study if the $\overline{\rm BHAR}$–Σ_1 relation is a more fundamental relation than the $\overline{\rm BHAR}$–$M_\star$ relation among SF non-BD galaxies. In Section 3.2, we will study if the $\overline{\rm BHAR}$–Σ_1 relation also exists among SF BD galaxies. In Section 3.3, we will first study if the $\overline{\rm BHAR}$–Σ_1 relation among SF non-BD galaxies is the same $\overline{\rm BHAR}$–Σ_1 relation among SF BD galaxies, and if the $\overline{\rm BHAR}$–Σ_1 relation that could apply to all SF galaxies seamlessly is a more fundamental relation than either of the $\overline{\rm BHAR}$–$M_\star$ or $\overline{\rm BHAR}$–SFR relations. We will then study the properties of the $\overline{\rm BHAR}$–Σ_1 relation and its cosmic evolution.

[5]For the subsamples utilized in this work, the contribution from XRBs makes up ≈1–10 per cent of the total X-ray emission, so that our analyses should not be affected materially by uncertainties related to the XRB modelling.

[6]Though it has been argued that for BHs accreting at low Eddington ratios or extremely high Eddington ratios, ϵ can be much smaller than 0.1 (e.g. Abramowicz & Fragile 2013; Yuan & Narayan 2014), observational constraints suggest that $\epsilon \gtrsim 0.1$ holds for most of cosmic BH growth (e.g. Brandt & Alexander 2015; Shankar et al. 2020).

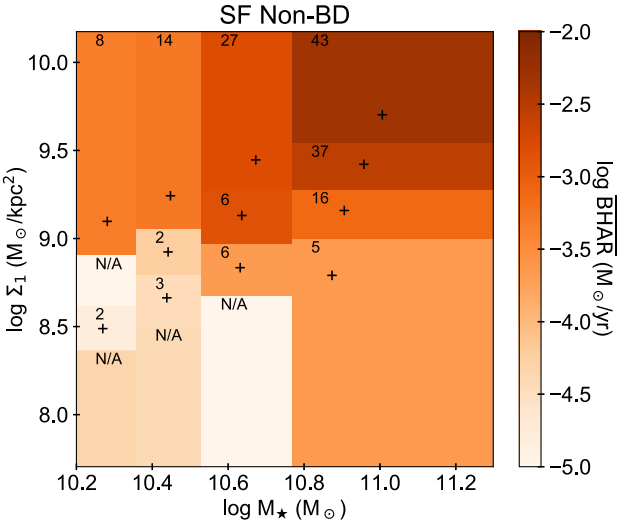

Figure 4. Colour-coded $\overline{\mathrm{BHAR}}$ in different bins of $M_\star$ and Σ_1 for galaxies in the SF non-BD sample. Each 2D bin contains ≈370 sources. The black plus sign indicates the median $M_\star$ and Σ_1 of the sources in each bin. For each bin, the number of X-ray detected galaxies is listed. For bins where $\overline{\mathrm{BHAR}}$ does not have a lower limit > 0 from bootstrapping or the number of X-ray detected galaxies is less than 2, 'N/A' is shown instead.

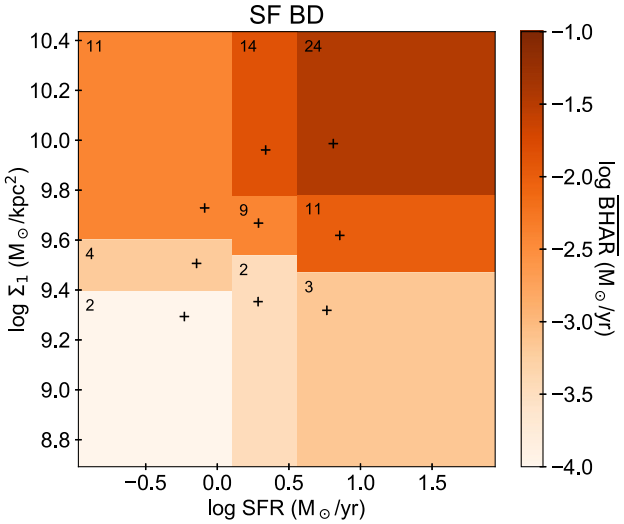

Figure 5. Colour-coded $\overline{\mathrm{BHAR}}$ in different bins of SFR and Σ_1 for galaxies in the SF BD sample. Each 2D bin contains ≈110 sources. The black plus sign indicates the median SFR and Σ_1 of the sources in each bin. For each bin, the number of X-ray detected galaxies is listed.

Table 2. *p*-values (significances) of PCOR analyses for the SF non-BD sample.

Relation	SF non-BD Pearson	Spearman
$\overline{\mathrm{BHAR}}$–Σ_1	**2×10^{-5} (3.8σ)**	**2×10^{-5} (3.7σ)**
$\overline{\mathrm{BHAR}}$–$M_\star$	0.12 (1.6σ)	0.03 (2.1σ)

Table 3. *p*-values (significances) of PCOR analyses for the SF BD sample.

Relation	SF BD Pearson	Spearman
$\overline{\mathrm{BHAR}}$–Σ_1	**5×10^{-5} (4.1σ)**	**3×10^{-4} (3.7σ)**
$\overline{\mathrm{BHAR}}$–SFR	4×10^{-3} (2.8σ)	**2×10^{-3} (3.1σ)**
$\overline{\mathrm{BHAR}}$–Σ_1	**9×10^{-4} (3.3σ)**	**1×10^{-3} (3.2σ)**
$\overline{\mathrm{BHAR}}$–$M_\star$	0.33 (1.0σ)	0.39 (0.9σ)

3.1 A $\overline{\mathrm{BHAR}}$–Σ_1 relation that is more fundamental than the $\overline{\mathrm{BHAR}}$–$M_\star$ relation among SF non-BD galaxies

Ni et al. (2019) found that the $\overline{\mathrm{BHAR}}$–Σ_1 relation among SF non-BD galaxies is not likely to be a secondary manifestation of the $\overline{\mathrm{BHAR}}$–$M_\star$ relation, and it is plausible that the $\overline{\mathrm{BHAR}}$–Σ_1 relation is indeed more fundamental than the $\overline{\mathrm{BHAR}}$–$M_\star$ relation. In this section, we test the significance of the $\overline{\mathrm{BHAR}}$–Σ_1 ($\overline{\mathrm{BHAR}}$–$M_\star$) relation when controlling for $M_\star$ (Σ_1) among galaxies in the SF non-BD sample with PCOR analyses. If we find a significant $\overline{\mathrm{BHAR}}$–Σ_1 relation when controlling for $M_\star$ but do not find a significant $\overline{\mathrm{BHAR}}$–$M_\star$ relation when controlling for Σ_1, we can conclude that the $\overline{\mathrm{BHAR}}$–Σ_1 relation is more fundamental than the $\overline{\mathrm{BHAR}}$–$M_\star$ relation among SF non-BD galaxies.

We bin galaxies in the SF non-BD sample based on both $M_\star$ and Σ_1 and calculate $\overline{\mathrm{BHAR}}$ for each bin. The bins are chosen to include approximately the same numbers of sources (≈370; see Fig. 4 for the 2D bins). Bins where $\overline{\mathrm{BHAR}}$ does not have a lower limit >0 or the number of X-ray detected galaxies is less than 2 (which will introduce large uncertainty into the estimated $\overline{\mathrm{BHAR}}$) will be excluded from the PCOR analyses. We input the median log $M_\star$, median log Σ_1, and log $\overline{\mathrm{BHAR}}$ of valid bins to PCOR.R in the R statistical package (Kim 2015), and the significance levels of the $\overline{\mathrm{BHAR}}$–Σ_1 ($\overline{\mathrm{BHAR}}$–$M_\star$) relation when controlling for $M_\star$ (Σ_1) with both the Pearson and Spearman statistics are calculated. The PCOR test results are summarized in Table 2. The parametric Pearson statistic is used to select significant results (we note that both the $\overline{\mathrm{BHAR}}$–$M_\star$ and $\overline{\mathrm{BHAR}}$–Σ_1 relations are roughly linear in log–log space; see Ni et al. 2019; Yang et al. 2019 for details), and the non-parametric Spearman statistic is also listed for reference. We can see from Table 2 that the $\overline{\mathrm{BHAR}}$–Σ_1 relation turns out to be more fundamental than the $\overline{\mathrm{BHAR}}$–$M_\star$ relation among SF non-BD galaxies. Our results do not qualitatively change with different binning approaches (see Appendix D for details).

3.2 The existence of a $\overline{\mathrm{BHAR}}$–Σ_1 relation among SF BD galaxies

We test the significance of the $\overline{\mathrm{BHAR}}$–Σ_1 relation when controlling for SFR among galaxies in the SF BD sample with PCOR analyses, as Yang et al. (2019) concluded that $\overline{\mathrm{BHAR}}$ among BD galaxies mainly correlates with SFR. We bin galaxies in the SF BD sample based on both SFR and Σ_1 and calculate $\overline{\mathrm{BHAR}}$ for each bin. The bins are chosen to include approximately the same numbers of sources (≈110; see Fig. 5 for the 2D bins). We input the median log SFR, median log Σ_1, and log $\overline{\mathrm{BHAR}}$ of valid bins to PCOR.R, and the significance levels of the $\overline{\mathrm{BHAR}}$–Σ_1 ($\overline{\mathrm{BHAR}}$–SFR) relation when controlling for SFR (Σ_1) with both the Pearson and Spearman statistics are calculated. The PCOR test results are summarized in Table 3.

From the PCOR test results, we can see that the $\overline{\mathrm{BHAR}}$–Σ_1 relation is significant when controlling for SFR, suggesting the important role of Σ_1 in predicting the amount of BH growth. The $\overline{\mathrm{BHAR}}$–SFR relation when controlling for Σ_1, at the same time, does not satisfy the 3σ criterion we adopted in Section 1 for the Pearson statistic to select significant correlations (though it is marginally significant). We

note again that our results do not qualitatively change with different binning approaches (see Appendix D for details). We also use the PCOR analyses to assess the significance levels of the $\overline{\rm BHAR}$–Σ_1 relation when controlling for $M_\star$ in a similar manner, and the results are listed in Table 3. The $\overline{\rm BHAR}$–Σ_1 relation remains significant, demonstrating that the observed $\overline{\rm BHAR}$–Σ_1 relation in the SF BD sample is not simply a manifestation of the $\overline{\rm BHAR}$–$M_\star$ relation. Thus, we can conclude that the $\overline{\rm BHAR}$–Σ_1 relation exists among SF BD galaxies. We note that our findings do not challenge the existence of the $\overline{\rm BHAR}$–SFR relation among BD galaxies in general (see Appendix E).

3.3 A $\overline{\rm BHAR}$–Σ_1 relation among all SF galaxies

We have confirmed the $\overline{\rm BHAR}$–Σ_1 relation in both the SF non-BD sample (see Section 3.1) and the SF BD sample (see Section 3.2). We will now study if the $\overline{\rm BHAR}$–Σ_1 relation among SF BD galaxies and the $\overline{\rm BHAR}$–Σ_1 relation among SF non-BD galaxies make consistent predictions at a given Σ_1, so that no ad hoc morphological division among SF galaxies is needed to study this relation. As the SF BD sample and the SF non-BD sample are selected with different $M_\star$ and z criteria (and only the SF non-BD sample is a mass-complete sample), we use the 355 SF BD galaxies with $\log M_\star > 10.2$ at $z < 0.8$ to perform the comparison. For each of these 355 galaxies, we select two galaxies from the larger SF non-BD sample that have the closest Σ_1 values to it (not allowing duplications) to constitute a comparison sample. We find that the $\log \overline{\rm BHAR}$ of these 355 SF BD galaxies is $-2.62^{+0.12}_{-0.16}$, and the $\log \overline{\rm BHAR}$ of SF non-BD galaxies in the comparison sample is $-2.41^{+0.11}_{-0.15}$, showing the consistent predictions of the $\overline{\rm BHAR}$–Σ_1 relation among SF BD galaxies and SF non-BD galaxies.[7]

We will now study this $\overline{\rm BHAR}$–Σ_1 relation that does not depend on morphological classes utilizing the ALL SF sample, which is constituted of all SF galaxies with $\log M_\star > 10.2$ at $z < 0.8$. This sample of SF galaxies is mass complete, so the derived $\overline{\rm BHAR}$–Σ_1 relation will not be significantly affected by the cosmic evolution of this relation. We use PCOR analyses to assess if the $\overline{\rm BHAR}$–Σ_1 relation in the ALL SF sample is still more fundamental than the $\overline{\rm BHAR}$–$M_\star$ relation. The 2D bins in the Σ_1 versus $M_\star$ plane that are utilized for PCOR analyses are presented in Fig. 6. As expected from the dominant number (≈94 per cent) of SF non-BD galaxies in the sample, the $\overline{\rm BHAR}$–Σ_1 relation is significant when controlling for $M_\star$, and the $\overline{\rm BHAR}$–$M_\star$ relation is not significant when controlling for Σ_1 (see Table 4). This result does not qualitatively change with different binning approaches (see Appendix D for details). We also perform the PCOR analyses in a similar manner for Σ_1 and SFR, and it turns out that the $\overline{\rm BHAR}$–Σ_1 relation is more fundamental than the $\overline{\rm BHAR}$–SFR relation (see Table 4).

To study the properties of the $\overline{\rm BHAR}$–Σ_1 relation, we divide galaxies in the ALL SF sample into Σ_1 bins with approximately the same number of X-ray detected galaxies (≈10) per bin, and calculate $\overline{\rm BHAR}$ and its 1σ confidence interval for each bin. In Fig. 7, we plot $\overline{\rm BHAR}$ of these bins as a function of the median Σ_1 value of each bin. We use the PYTHON package EMCEE (Foreman-Mackey et al. 2013) to fit a log-linear model to the $\overline{\rm BHAR}$–Σ_1 relation, where the maximum likelihood method is implemented by the Markov chain Monte Carlo

[7]We do not directly derive the $\overline{\rm BHAR}$–Σ_1 relation among SF BD galaxies and SF non-BD galaxies separately and compare, as quantifying the $\overline{\rm BHAR}$–Σ_1 relation solely among SF BD galaxies will suffer from uncertainty that is too large to conduct any meaningful comparison.

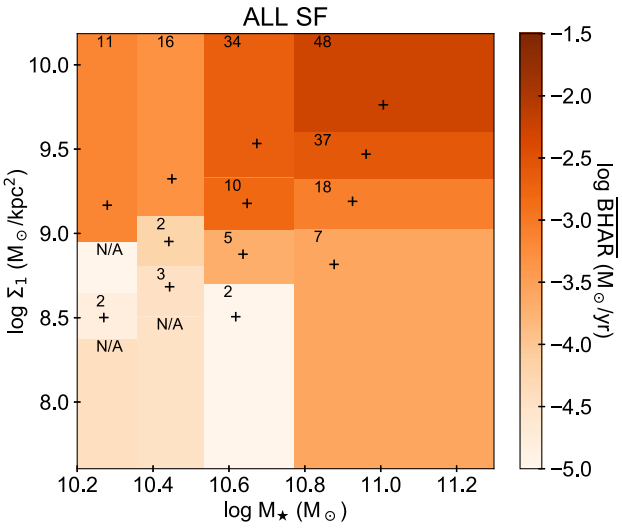

Figure 6. Colour-coded $\overline{\rm BHAR}$ in different bins of $M_\star$ and Σ_1 for galaxies in the ALL SF sample. Each 2D bin contains ≈390 sources. The black plus sign indicates the median $M_\star$ and Σ_1 of the sources in each bin. For each bin, the number of X-ray detected galaxies is listed. For bins where $\overline{\rm BHAR}$ does not have a lower limit >0 from bootstrapping or the number of X-ray detected galaxies is less than 2, 'N/A' is shown instead.

Table 4. *p*-values (significances) of PCOR analyses for the ALL SF sample.

Relation	ALL SF Pearson	Spearman
$\overline{\rm BHAR}$–Σ_1	$\mathbf{2 \times 10^{-5}}$ **(4.2σ)**	$\mathbf{2 \times 10^{-4}}$ **(3.7σ)**
$\overline{\rm BHAR}$–$M_\star$	0.28 (1.1σ)	0.14 (1.5σ)
$\overline{\rm BHAR}$–Σ_1	$\mathbf{6 \times 10^{-5}}$ **(4.0σ)**	$\mathbf{9 \times 10^{-6}}$ **(4.4σ)**
$\overline{\rm BHAR}$–SFR	0.46 (0.7σ)	0.18 (1.3σ)

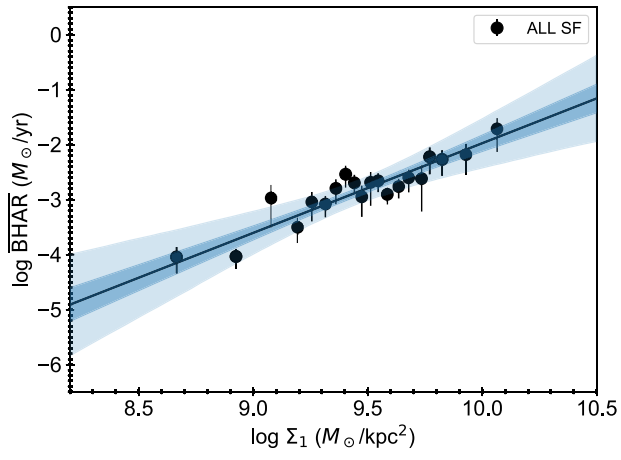

Figure 7. The $\overline{\rm BHAR}$–Σ_1 relation among SF galaxies. Galaxies in the ALL SF sample are divided into bins according to their Σ_1 values, with ≈10 X-ray detected galaxies in each bin. The horizontal position of each data point indicates the median Σ_1 of the sources in the bin; the error bars represent the 1σ confidence interval of $\overline{\rm BHAR}$ from bootstrapping. The black solid line and the dark/light blue shaded region represent the best-fitting $\overline{\rm BHAR}$–Σ_1 relation and the $1\sigma/3\sigma$ pointwise confidence intervals on the regression line.

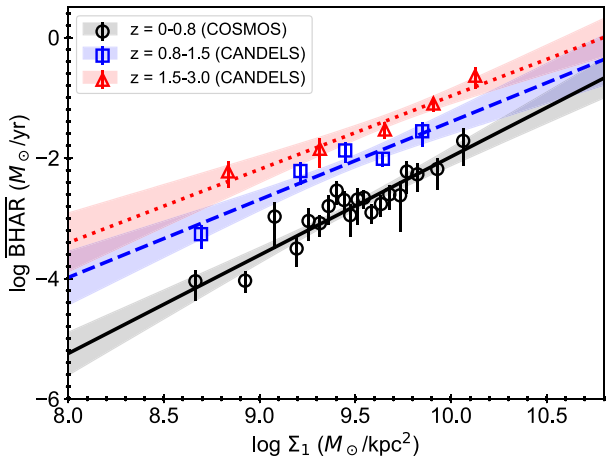

Figure 8. The cosmic evolution of the $\overline{\mathrm{BHAR}}$–Σ_1 relation among SF galaxies. z = 0–0.8 galaxies from COSMOS, z = 0.8–1.5 galaxies from CANDELS, and z = 1.5–3 galaxies from CANDELS with $\log M_\star > 10.2$ are divided into several bins according to their Σ_1 values with approximately the same number of X-ray detected galaxies in each bin, represented by the black circles, blue squares, and red triangles, respectively. The horizontal position of each data point indicates the median Σ_1 of the sources in the bin; the error bars represent the 1σ confidence interval of $\overline{\mathrm{BHAR}}$ from bootstrapping. The black solid line and the grey shaded region represent the best-fitting $\overline{\mathrm{BHAR}}$–Σ_1 relation and its 1σ pointwise confidence interval for z = 0–0.8 galaxies; the blue dashed line and the blue shaded region are for the z = 0.8–1.5 galaxies; and the red dotted line and the red shaded region are for the z = 1.5–3 galaxies.

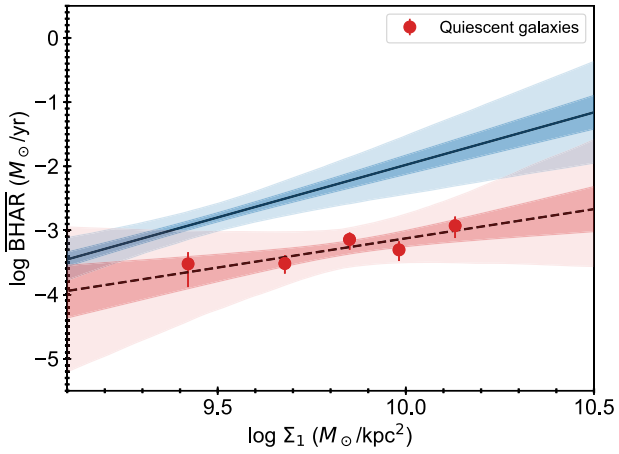

Figure 9. The $\overline{\mathrm{BHAR}}$–Σ_1 relation among quiescent galaxies. 3400 quiescent galaxies with $\log M_\star > 10.2$ at $z < 0.8$ are divided into bins according to their Σ_1 values, with ≈20 X-ray detected galaxies in each bin. The horizontal position of each data point indicates the median Σ_1 of the sources in the bin; the error bars represent the 1σ confidence interval of $\overline{\mathrm{BHAR}}$ from bootstrapping. The black dashed line and the dark/light red shaded region represent the best-fitting $\overline{\mathrm{BHAR}}$–Σ_1 relation among quiescent galaxies and the $1\sigma/3\sigma$ pointwise confidence intervals on the regression line, respectively. The black solid line and the dark/light blue shaded region are adopted from Fig. 7, representing the best-fitting $\overline{\mathrm{BHAR}}$–Σ_1 relation among SF galaxies in the same $M_\star$ and z ranges and the $1\sigma/3\sigma$ pointwise confidence intervals on the regression line, respectively. At a given Σ_1, the $\overline{\mathrm{BHAR}}$ values of quiescent galaxies are below the 3σ lower limit of the best-fitting $\overline{\mathrm{BHAR}}$–Σ_1 relation among SF galaxies, and the best-fitting slope of the $\log\overline{\mathrm{BHAR}}$–$\log\Sigma_1$ relation among quiescent galaxies is much flatter compared with the best-fitting slope among SF galaxies.

Ensemble sampler. By fitting all the data points in Fig. 7, we obtain

$$\log\overline{\mathrm{BHAR}} = (1.6 \pm 0.2) \times \log\Sigma_1 + (-18.3 \pm 2.6). \quad (5)$$

The best-fitting model and its $1\sigma/3\sigma$ pointwise confidence intervals are also shown in Fig. 7.

Two subsamples of $H_{160\mathrm{W}} < 24.5$ SF galaxies with $\log M_\star > 10.2$ in the CANDELS fields drawn from the Ni et al. (2019) sample will also be utilized to probe how the $\overline{\mathrm{BHAR}}$–Σ_1 relation evolves over the history of the Universe: one subsample is constituted of ≈1500 SF galaxies at z = 0.8–1.5 (where Σ_1 values are inferred from $J_{125\mathrm{W}}$-band light profiles), and the other subsample is constituted of ≈1800 SF galaxies at z = 1.5–3 (where Σ_1 values are inferred from $H_{160\mathrm{W}}$-band light profiles). Though the utilized *HST* bands are different, we note that the light profiles are always measured in the rest-frame optical. $H_{160\mathrm{W}} < 24.5$ galaxies in the CANDELS fields are mass complete at $\log M_\star > 10.2$ up to z = 3, so these subsamples are also mass-complete samples. For each subsample, we divide objects into Σ_1 bins,[8] and calculate $\overline{\mathrm{BHAR}}$ and its 1σ confidence interval for each bin. The $\overline{\mathrm{BHAR}}$ values of these bins as a function of Σ_1 are shown in Fig. 8 along with the data points in Fig. 7 (which show $\overline{\mathrm{BHAR}}$ as a function of Σ_1 in the ALL SF sample that is constituted by z = 0–0.8 SF galaxies in the COSMOS field). We then use the EMCEE package to fit a log-linear model to the $\overline{\mathrm{BHAR}}$–Σ_1 relation among each subsample, as we did for the ALL SF sample. The best-fitting $\overline{\mathrm{BHAR}}$–Σ_1 relations of SF galaxies in different redshift ranges are presented together in Fig. 8. We can see that while the slope of the best-fitting log-linear model does not change significantly with redshift, for a given Σ_1 value, the expected $\overline{\mathrm{BHAR}}$ is higher at higher redshift: $\overline{\mathrm{BHAR}}$ at z = 1.5–3 is higher than that at z = 0–0.8 by ∼1 dex when controlling for Σ_1.

[8] As $M_\star$ values utilized in Ni et al. (2019) to calculate Σ_1 are also measured with parametric SFHs that tend to underestimate the true $M_\star$ (Leja et al. 2019), we apply a ≈0.15 dex correction to Σ_1 values of galaxies in the two CANDELS subsamples to maintain consistency with the $M_\star$ scheme utilized in this paper.

4 DISCUSSION

4.1 What is implied by the apparent link between BH growth and host-galaxy compactness?

4.1.1 The link between BH growth and the central gas density of host galaxies: a common origin of the gas in the vicinity of the BH and the central ∼kpc?

In Section 3, we confirmed a $\overline{\mathrm{BHAR}}$–Σ_1 relation that is more fundamental than either the $\overline{\mathrm{BHAR}}$–$M_\star$ or $\overline{\mathrm{BHAR}}$–SFR relation among SF galaxies, which reveals the link between long-term average BH growth and host-galaxy compactness. This $\overline{\mathrm{BHAR}}$–Σ_1 relation is only significant among SF galaxies (Ni et al. 2019). If we plot $\overline{\mathrm{BHAR}}$ as a function of Σ_1 for quiescent galaxies (see Fig. 9), we can see that $\overline{\mathrm{BHAR}}$ does not vary significantly with Σ_1 among quiescent galaxies, and the fitted slope (0.9 ± 0.5) of the $\log\overline{\mathrm{BHAR}}$–$\log\Sigma_1$ relation among quiescent galaxies is flatter compared with the slope among SF galaxies, being consistent with zero at a ≈2σ level. This led us to speculate that the $\overline{\mathrm{BHAR}}$–Σ_1 relation reflects a link between BH growth and the central gas density (on the ∼kpc scale) of host galaxies (among quiescent galaxies, Σ_1 cannot effectively trace the central gas

density).[9] The observed cosmic evolution of the $\overline{\mathrm{BHAR}}$–Σ_1 relation in Section 3.3 supports our speculation: observations show that the average (molecular) gas fraction among galaxies increases by a factor of ∼10 from $z \approx 0.4$ to $z \approx 2$ (e.g. Schinnerer et al. 2016; Tacconi et al. 2018), and this could well explain our observed result that for a given Σ_1, $\overline{\mathrm{BHAR}}$ increases by a factor of ∼10 from $z = 0$–0.8 to $z = 1.5$–3.

If we can approximate Σ_1 as a function of gas surface density (Σ_{gas}) in the central ∼kpc of galaxies, we will be able to convert the $\overline{\mathrm{BHAR}}$–Σ_1 relation to a $\overline{\mathrm{BHAR}}$–Σ_{gas} relation. According to the Kennicutt–Schmidt law (e.g. Kennicutt 1998b), the SFR surface density (Σ_{SFR}) is tightly linked with Σ_{gas} with a power-law index $\approx 1.4 \pm 0.15$. Also, observations and simulations suggest that Σ_{SFR} on the ∼kpc scale correlates with $M_\star$ density ($\Sigma_{M_\star}$) on the same scale in SF regions (e.g. Cano-Díaz et al. 2016; Hsieh et al. 2017; Trayford & Schaye 2019; Hani et al. 2020), though the reported slope values (β) of the $\log \Sigma_{\mathrm{SFR}}$–$\log \Sigma_{M_\star}$ relation vary from ≈0.7 to ≈1. Given all these findings, we can approximate Σ_1 as a power-law function of Σ_{gas} in the central ∼1 kpc of galaxy with an index of $\approx 1.4/\beta$, suggesting that the $\overline{\mathrm{BHAR}}$–Σ_{gas} relation has a power-law index of ∼2–4. Further studies that utilize high-resolution ALMA observations to resolve the gas density will help to quantify directly the relation between Σ_1 and Σ_{gas}, thus making the conversion from the $\overline{\mathrm{BHAR}}$–Σ_1 relation to a $\overline{\mathrm{BHAR}}$–Σ_{gas} relation more reliable; with ALMA observations of a sample of 32 galaxies at $z \lesssim 0.1$, a tight relation between Σ_{gas} and $\Sigma_{M_\star}$ has already been suggested in Lin et al. (2019), and a larger sample size is needed for further quantification of this relation. Alternatively, future accumulation of ALMA observations in combination with deep X-ray observations will enable us to probe the $\overline{\mathrm{BHAR}}$–Σ_{gas} relation directly.

Assuming Σ_1 serves as an indicator of Σ_{gas}, the $\overline{\mathrm{BHAR}}$–Σ_1 relation may indicate that gas in the vicinity of the BH that will be accreted has the same origin as gas in the central ∼kpc part of galaxies. It is plausible that gas could be transported from the inner ≈1 kpc of galaxies all the way to the torus and accretion disc via gravitational instabilities (see Storchi-Bergmann & Schnorr-Müller 2019 and references therein). If Σ_{gas} (on kpc scales) correlates with the ambient gas density (ρ) of BHs (on pc to sub-kpc scales) well, the relation between BH growth and ρ may be quantitatively examined. However, while we can convert the $\overline{\mathrm{BHAR}}$–Σ_1 relation to a $\overline{\mathrm{BHAR}}$–Σ_{gas} relation, this does not necessarily mean the dependence of BH growth on ρ can be directly inferred.

BH growth may depend on other factors that also correlate with Σ_1. Bondi-type accretion models (e.g. Bondi 1952; Springel, Di Matteo & Hernquist 2005) predict that the amount of BH growth should be approximately proportional to $M_{\mathrm{BH}}^2 \rho c_{\mathrm{s}}^{-3}$ (assuming that the gas has negligible velocity relative to the BH as an initial condition; c_{s} is the sound speed in the gas), and both M_{BH} and c_{s} correlate with Σ_1 (though with considerable scatters).[10] We can roughly infer the correlation between Σ_1 and M_{BH} from the M_{BH}–$M_\star$ relation and the Σ_1–$M_\star$ relation among the general galaxy population. The power-law index of the M_{BH}–$M_\star$ relation observed in the local Universe is ≈1.05 (e.g. McConnell & Ma 2013; Reines & Volonteri 2015); we note that this relation is not very tight, with a scatter of ≈0.55 dex. Also, this M_{BH}–$M_\star$ relation does not seem to have significant cosmic evolution at $z < 2$ (e.g. Kormendy & Ho 2013; Sun et al. 2015; Ding et al. 2020; Suh et al. 2020). The power-law index of the Σ_1–$M_\star$ relation is ≈1.1 in the ALL SF sample. We thus infer that Σ_1 can be expressed as a power-law function of M_{BH} with an index close to one (though with a considerable scatter). As c_{s}^2 scales with the temperature of the medium, it should also scale with M/R assuming virial equilibrium, where M and R are the mass and radius of the gravitationally bound system in the vicinity of the BH. It has been suggested that M/R scales with $M_\star/(K_v(n) r_{\mathrm{e}})$ (see section 1 of Taylor et al. 2010), where

$$K_v(n) \cong \frac{73.32}{10.465 + (n - 0.94)^2} + 0.954. \quad (6)$$

Through fitting objects in our ALL SF sample, we found that Σ_1 could be expressed as a power-law function of $M_\star/(K_v(n) r_{\mathrm{e}})$ with an index of ∼1.3. Utilizing this conversion, c_{s}^{-3} should be proportional to $\sim {\Sigma_1}^{-1.1}$ (as c_{s}^2 is proportional to M/R when assuming virial equilibrium, and M/R scales with $M_\star/(K_v(n) r_{\mathrm{e}})$). Thus, if Bondi-type accretion models can well-approximate BH growth among SF galaxies, and if Σ_{gas} correlates well with ρ, we should observe a $\overline{\mathrm{BHAR}}$–Σ_1 relation with an index of ∼1.4–1.6 (as ${M_{\mathrm{BH}}}^2 \propto {\Sigma_1}^2$, $\rho \propto {\Sigma_1}^{\beta/1.4}$, and $c_{\mathrm{s}}^{-3} \propto {\Sigma_1}^{-1.1}$), which is consistent with the best-fitting log-linear model in Section 3.3 that has a slope of 1.6 ± 0.2.

4.1.2 An indicated role of the host-galaxy potential well in feeding BHs?

Alternatively, the $\overline{\mathrm{BHAR}}$–Σ_1 relation may reflect a link between BH growth and the host-galaxy potential well depth at a certain gas content among SF galaxies. We note that Σ_1 is tightly correlated with the inferred central velocity dispersion (σ_{inf}; Bezanson et al. 2011) of galaxies:

$$\sigma_{\mathrm{inf}} = \sqrt{\frac{G M_\star}{K_\star(n) r_{\mathrm{e}}}}, \quad (7)$$

where

$$K_\star(n) = 0.557 \times K_v(n). \quad (8)$$

At $z \sim 0$, σ_{inf} has proven to be a good approximation of the true central velocity dispersion (σ; Bezanson et al. 2011), which measures the potential well depth of galaxies.[11] In the first panel of Fig. 10, we show galaxies in the ALL SF sample in the Σ_1 versus σ_{inf} plane. We can see that most of these galaxies, and especially the X-ray detected galaxies, are 'degenerate' in the Σ_1 versus σ_{inf} space (i.e. their Σ_1 values are tightly correlated with their σ_{inf} values). It is possible that Σ_1 actually serves as a proxy for the central velocity dispersion when predicting BH growth in our study: we find that

[9] We note that there is still limited SF activity among the quiescent galaxies we selected (see Section 2.4), so that there may still be a shallow trend between Σ_1 and the central gas density (though with large scatter), which could explain the observed shallow slope of the $\log \overline{\mathrm{BHAR}}$–$\log \Sigma_1$ relation in Fig. 9.

[10] While we have necessarily assumed zero angular momentum here with the Bondi-type accretion model (that has been suggested to be a reliable approximation of BH accretion), we note that in real cases, the accretion of gas with significant angular momentum on to the BH is far more complicated than the simple picture proposed here.

[11] In Bezanson et al. (2011), the comparison between σ_{inf} and σ is mainly performed using a large sample of the Sloan Digital Sky Survey (SDSS) galaxies at $z \sim 0$ where a good agreement is confirmed. At high redshift, only tens of objects have measurements of σ (with large error bars). Their σ_{inf} values are in general consistent with σ measurements. Bezanson et al. (2011) thus assume that σ_{inf} can also be a good approximation of σ at high redshift. This is also the underlying assumption when we use σ_{inf} to approximate σ for objects in our sample.

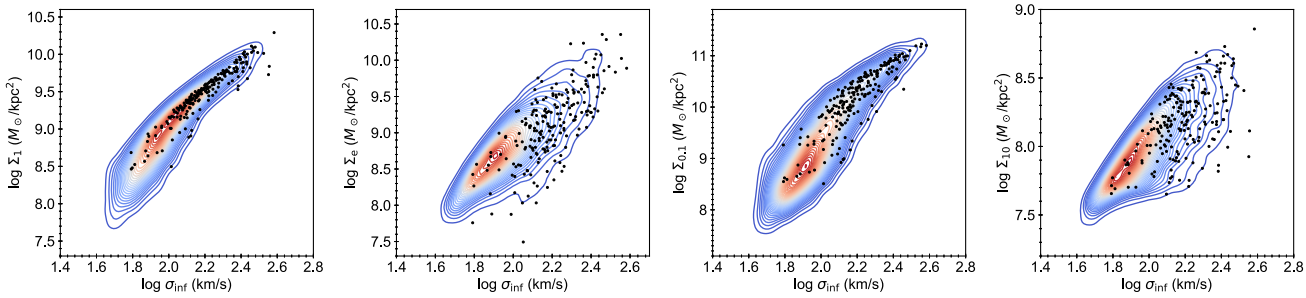

Figure 10. Left to right: 2D kernel density estimation (KDE) plot of Σ_1, Σ_e, $\Sigma_{0.1}$, and Σ_{10} versus σ_{inf} of galaxies in the ALL SF sample. X-ray detected galaxies are represented by the black dots. Note the correlation between σ_{inf} and Σ_1 is tighter than the correlations between σ_{inf} and other compactness parameters shown.

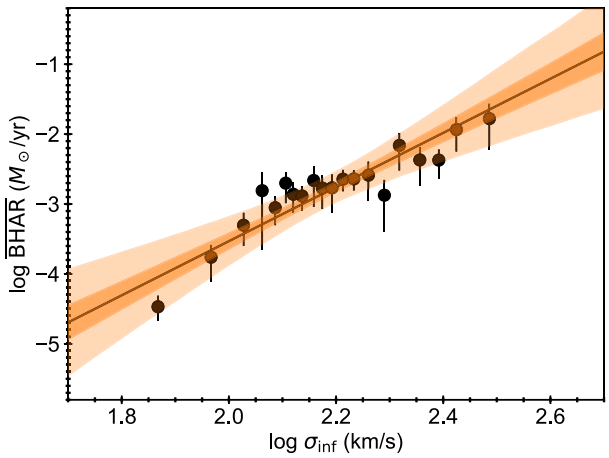

Figure 11. $\overline{\text{BHAR}}$ as a function of σ_{inf} among SF galaxies. Galaxies in the ALL SF sample are divided into bins according to their σ_{inf} values, with ≈10 X-ray detected galaxies in each bin. The horizontal position of each data point indicates the median σ_{inf} of the sources in the bin; the error bars represent the 1σ confidence interval of $\overline{\text{BHAR}}$ from bootstrapping. The black solid line and the dark/light orange shaded region represent the best-fitting $\overline{\text{BHAR}}$–σ_{inf} relation and the $1\sigma/3\sigma$ pointwise confidence intervals on the regression line, respectively.

all the analysis results in Section 3 do not change qualitatively if we replace Σ_1 with σ_{inf}. If so, the effectiveness of Σ_1 among all possible compactness parameters could naturally be explained. Ni et al. (2019) found that Σ_1 is a better indicator of BH growth than the surface mass density (Σ_e); also, if we calculate the projected central mass density within 0.1 kpc ($\Sigma_{0.1}$) or 10 kpc (Σ_{10}) by extrapolating the measured Sérsic profiles similarly to the approach presented in equation (2), we find that Σ_1 is also a better indicator compared with them. It is interesting and reasonable to question why it is the mass density in the central ∼1 kpc part that matters most. In the last three panels of Fig. 10, we plot Σ_e, $\Sigma_{0.1}$, and Σ_{10} versus σ_{inf} for galaxies in the ALL SF sample. None of these quantities are as tightly correlated with σ_{inf} as Σ_1 (see Fig. 10): it might be the case that the mass density in the central ∼1 kpc part matters most simply because it is the best representative of the central velocity dispersion among all the compactness parameters examined (see Fang et al. 2013 for the tight correlation between Σ_1 and the central velocity dispersion of SDSS galaxies).

In Fig. 11, we present the $\overline{\text{BHAR}}$–σ_{inf} relation among SF galaxies. This $\overline{\text{BHAR}}$–σ_{inf} relation suggests that the host-galaxy potential well may play a fundamental role in feeding BHs among SF galaxies where cold gas is abundant.[12] In this scenario, the link between BH growth and Σ_{gas} in the central ∼1 kpc still exists, though it actually *manifests* the relation between BH growth and host-galaxy potential well depth at a given gas content. Fitting the data points in Fig. 11 with EMCEE, the best-fitting log-linear model of the $\overline{\text{BHAR}}$–σ_{inf} relation is

$$\log \overline{\text{BHAR}} = (3.9 \pm 0.5) \times \sigma_{inf} + (-11.3 \pm 1.1). \quad (9)$$

As the 1σ uncertainty of the slope is large, the exact form of the $\overline{\text{BHAR}}$–σ_{inf} relation remains unclear. It has been suggested that AGNs can feed efficiently from surrounding dense gas clumps, at rates close to the dynamical rate $\dot{M}_{dyn}$ (assuming that the gas is initially in rough virial equilibrium; Zubovas & King 2019):

$$\dot{M}_{dyn} \propto \frac{f_g \sigma^3}{G}, \quad (10)$$

where f_g is the gas fraction in the galaxy that could explain the cosmic evolution of the $\overline{\text{BHAR}}$–Σ_1 (or the $\overline{\text{BHAR}}$–σ_{inf}) relation. Among quiescent galaxies that lack gas, $\dot{M}_{dyn}$ cannot be achieved, so that $\overline{\text{BHAR}}$ does not have strong dependence on σ_{inf} (or Σ_1). The predicted slope (of 3) is within the $\sim 2\sigma$ confidence interval of the fitting result. A larger sample of galaxies/AGNs will be needed to provide further constraints on the relation that could validate or rule out this scenario, and provide more insights into the BH feeding mechanism among SF galaxies.

While the observed $\overline{\text{BHAR}}$–Σ_1 relation may suggest the role of the host-galaxy potential well in feeding the BH, we note that the M_{BH}–σ relation observed among local bulges may suggest the role of the host-galaxy potential well in 'shutting off' the BH growth (AGN feedback via outflows is one possible way to achieve this 'shut-off' process; e.g. Silk & Rees 1998; King 2005; Murray et al. 2005), further indicating the connection between the host-galaxy potential well and the BH growth.

We also note that, from the side of galaxy evolution, Σ_1 (or σ) is linked with the colour (or specific SFR) of galaxies (e.g. Fang et al. 2013; Whitaker et al. 2017), and serves as a good predictor of quiescence. AGN activity reaches the high-point among high-Σ_1 SF galaxies that become quiescent later on (see Section 3.3; also see Kocevski et al. 2017), which indicates that there is a potential link between AGNs and the quenching of galaxies: whatever process (i.e. AGN feedback, morphological quenching, and halo gas shock

[12]We note that the $\overline{\text{BHAR}}$–σ_{inf} relation is not necessarily 'responsible' for producing the M_{BH}–σ relation among local bulges. The M_{BH}–σ relation may simply mark the turning point where both the BH and galaxy cannot be fuelled efficiently (e.g. King 2005, 2010; Murray, Quataert & Thompson 2005).

heating) that quenches galaxies may also slow down the BH growth (see Fig. 9 for the BH growth among high-Σ_1 quiescent galaxies).

4.2 Potential connections between the $\overline{\mathrm{BHAR}}$–Σ_1 relation and the M_{BH}–M_{bulge} relation, and implications for BH 'monsters' among local bulges

In Section 3.2, we confirmed the $\overline{\mathrm{BHAR}}$–Σ_1 relation among SF BD galaxies, and we also verified that the $\overline{\mathrm{BHAR}}$–Σ_1 relation among all SF galaxies applies to BD galaxies and non-BD galaxies seamlessly in Section 3.3. The $\overline{\mathrm{BHAR}}$–Σ_1 relation and the M_{BH}–M_{bulge} relation may indeed reflect the same underlying link. As discussed in Section 4.1, this link may be the direct dependence of BH growth on the central ∼kpc gas density of host galaxies, or the dependence of BH growth on the host-galaxy potential well depth at a given gas content (which will also manifest a link between BH growth and Σ_{gas} on the ∼kpc scale). We will show below how the $\overline{\mathrm{BHAR}}$–Σ_1 relation and the M_{BH}–M_{bulge} relation quantitatively agree. Among ellipticals and classical bulges in the local Universe, the M_{BH}–M_{bulge} relation takes the form of

$$M_{\mathrm{BH}} \propto M_{\mathrm{bulge}}^{\alpha}, \tag{11}$$

and the reported values of α range from ≈1.2 (e.g. Kormendy & Ho 2013) to ≈1.4 (e.g. Reines & Volonteri 2015). If we assume that this relation also approximately holds true at higher redshift (see fig. 38c of Kormendy & Ho 2013) and take the (time) derivative of this formula, we obtain

$$\mathrm{d}M_{\mathrm{BH}} \propto M_{\mathrm{bulge}}^{\alpha-1} \times \mathrm{d}M_{\mathrm{bulge}}, \tag{12}$$

which suggests that

$$\overline{\mathrm{BHAR}} \propto M_{\mathrm{bulge}}^{\alpha-1} \times \mathrm{SFR}_{\mathrm{bulge}}, \tag{13}$$

where $\mathrm{SFR}_{\mathrm{bulge}}$ is the SFR of the bulge component. Through assuming that $\mathrm{SFR}_{\mathrm{bulge}}$ is approximately proportional to $\Sigma_{\mathrm{SFR,\,1\,kpc}}$, we can further express $\mathrm{SFR}_{\mathrm{bulge}}$ as a function of Σ_1: $\mathrm{SFR}_{\mathrm{bulge}} \propto {\Sigma_1}^{\beta}$, where β is the slope of the $\log \Sigma_{\mathrm{SFR}}$–$\log \Sigma_{M_\star}$ relation ($\beta \sim 0.7$–1; e.g. Cano-Díaz et al. 2016; Hsieh et al. 2017; Trayford & Schaye 2019; Hani et al. 2020).[13] We can also approximate M_{bulge} as a power-law function of Σ_1: through fitting all $\log M_\star > 10.2$ BD galaxies at $z < 0.8$ in our sample, we find that the power-law index is ∼1.6. We can then write the right-hand side of equation (13) as a pure function of Σ_1:

$$\overline{\mathrm{BHAR}} \propto \Sigma_1^{1.6\times(\alpha-1)} \times \Sigma_1^{\beta}. \tag{14}$$

Different combinations of α and β values predict the power-law index of the $\overline{\mathrm{BHAR}}$–Σ_1 relation to be ∼1.0–1.6, which is consistent with our derived index of 1.6 ± 0.2 in Section 3.3. Thus, it is plausible that the observed M_{BH}–M_{bulge} relation reflects the same underlying link as the $\overline{\mathrm{BHAR}}$–Σ_1 relation. This picture of the same underlying link for both the $\overline{\mathrm{BHAR}}$–Σ_1 and M_{BH}–M_{bulge} relations is also supported by the observed scatter of the M_{BH}–M_{bulge} relation. The Σ_1 values of SF BD galaxies in our sample at a given $M_\star$ have a scatter of ∼0.2 dex. Considering the $\overline{\mathrm{BHAR}}$–Σ_1 relation, we would expect a ∼0.3 dex scatter for the M_{BH}–M_{bulge} relation, which is the scatter observed in section 6.6.1 of Kormendy & Ho (2013).

It is plausible that the M_{BH}–M_{bulge} relation cannot characterize the BH 'monsters' (i.e. BHs found in local compact galaxies that have M_{BH} values much larger than expected from the M_{BH}–M_{bulge} relation) well simply because in cases where the bulge is so compact and the gas is so highly concentrated, the central ∼kpc gas density (or the central velocity dispersion that is tightly linked with compactness) cannot be well approximated by the SFR of the whole bulge. Our derived $\overline{\mathrm{BHAR}}$–Σ_1 relation in Section 3.3, at the same time, may manifest the underlying link better in ultracompact SF bulges, and it has the potential to explain the local BH 'monsters'. We will take NGC 4486B as an example, where the $\approx 6 \times 10^8$ $\mathrm{M}_\odot$ BH is 'overmassive' by ≈1.7 dex (Kormendy & Ho 2013). NGC 4486B has $r_{\mathrm{e}} \approx 0.2$ kpc and $n \approx 2.2$ (Kormendy et al. 2009). If we compare NGC 4486B with a typical local bulge that has $r_{\mathrm{e}} \approx 3$ kpc and $n \approx 3$, we find that the percentage of mass concentrated in the central 1 kpc of NGC 4486B is greater than that of a typical bulge by a factor of ≈5. This means that the Σ_1 value of NGC 4486B is larger than the typical Σ_1 value at the same M_{bulge} by ≈0.7 dex. If we assume this deviation approximately holds true during all BH-growth episodes of NGC 4486B, a ≈1.1 dex elevation in its M_{BH} compared with typical local bulges that have similar M_{bulge} values will be generated according to the derived $\overline{\mathrm{BHAR}}$–Σ_1 relation (see equation 9). We also note that for a given Σ_1, the expected amount of BH growth could increase by ≈1 dex when the redshift rises (see Fig. 8). If NGC 4486B is a 'relic' galaxy that had finished growing most of its M_{BH} by $z \sim 2$, an additional elevation of its M_{BH} by up to ≈1 dex compared with typical local bulges that have similar M_{bulge} values can be expected due to the cosmic evolution of BH growth at a given Σ_1: for these typical bulges, a significant fraction (∼50 per cent) of $M_\star$ is likely to be assembled at $z < 2$ (e.g. Thomas et al. 2005, 2010; De Lucia et al. 2006), suggesting a significant amount of BH mass assembly at $z < 2$. Taking all these into account, the ≈1.7 dex deviation in M_{BH} of NGC 4486B from the M_{BH}–M_{bulge} relation is understandable as BHs among SF galaxies follow the $\overline{\mathrm{BHAR}}$–Σ_1 relation.

5 CONCLUSIONS AND FUTURE WORK

Utilizing extensive multiwavelength observations in the COSMOS survey field, we have revealed and studied the dependence of BH growth on host-galaxy compactness represented by Σ_1 among SF galaxies. The main points from this paper are the following.

(i) We built a catalogue of $I_{\mathrm{F814W}} < 24$ galaxies at $z < 1.2$ from the COSMOS survey field (Section 2). We measured their $M_\star$ and SFR values utilizing UV-to-FIR photometry (Section 2.1 and Appendix A). We measured their structural parameters (Section 2.2 and Appendix B), and classify them as BD or non-BD galaxies (Section 2.3 and Appendix C) utilizing the high-resolution *HST* F814W mosaics. Drawing upon all these measurements, we compiled a sample of SF non-BD galaxies and a sample of SF BD galaxies, as well as an ALL SF sample regardless of morphology (Section 2.4). Σ_1 values of galaxies are calculated from $M_\star$ and

[13] If we fit the SFR–Σ_1 relation directly among the SF BD sample, we obtain a power-law index of $\approx 0.7 \pm 0.1$, consistent with the adopted β values. The scatter of the fitted $\log \mathrm{SFR}$–$\log \Sigma_1$ relation is ≈0.5 dex, and a significant fraction of this scatter could be attributed to the uncertainty associated with the $\mathrm{SFR}_{\mathrm{bulge}}$–$\Sigma_{\mathrm{SFR,\,1\,kpc}}$ relation, as the expected scatter associated with the $\log \Sigma_{\mathrm{SFR,\,1\,kpc}}$–$\log \Sigma_1$ relation is ∼0.2–0.3 dex (e.g. Cano-Díaz et al. 2016; Hsieh et al. 2017; Lin et al. 2019). While the assumption of $\mathrm{SFR}_{\mathrm{bulge}} \propto \Sigma_{\mathrm{SFR,\,1\,kpc}}$ automatically holds true when Σ_{SFR} is uniform across the bulge, Σ_{SFR} is not uniform in real cases (e.g. Nelson et al. 2012). Thanks to the compact sizes of bulges (on the kpc scale), we expect a considerable fraction of their star formation to be enclosed in their central 1 kpc regions. Thus, while Σ_{SFR} may be far from uniform, the assumed relation between $\mathrm{SFR}_{\mathrm{bulge}}$ and $\Sigma_{\mathrm{SFR,\,1\,kpc}}$ still roughly holds, though a considerable scatter is associated with this relation, which originates from the scatter in the fraction of SFR enclosed in the central 1 kpc region among SF BD galaxies.

structural parameters. Deep *Chandra* X-ray observations in the field are utilized to estimate $\overline{\mathrm{BHAR}}$ for samples of galaxies (see Section 2.5).

(ii) Utilizing PCOR analyses, we found that the $\overline{\mathrm{BHAR}}$–Σ_1 relation is more fundamental than the $\overline{\mathrm{BHAR}}$–$M_\star$ relation among SF non-BD galaxies (Section 3.1), as we observe a significant $\overline{\mathrm{BHAR}}$–Σ_1 relation when controlling for $M_\star$, while we do not observe a significant $\overline{\mathrm{BHAR}}$–$M_\star$ relation when controlling for Σ_1. We also found that the $\overline{\mathrm{BHAR}}$–Σ_1 relation is significant when controlling for SFR in the SF BD sample (Section 3.2), which suggests that the $\overline{\mathrm{BHAR}}$–Σ_1 relation also exists among SF BD galaxies.

(iii) We confirmed that the same $\overline{\mathrm{BHAR}}$–Σ_1 relation applies to both SF non-BD and SF BD galaxies, and this $\overline{\mathrm{BHAR}}$–Σ_1 relation is more fundamental than either the $\overline{\mathrm{BHAR}}$–$M_\star$ or $\overline{\mathrm{BHAR}}$–SFR relation among SF galaxies (Section 3.3). Our best-fitting $\log \overline{\mathrm{BHAR}}$–$\log \Sigma_1$ relation has a slope of 1.6 ± 0.2. While the slope of the $\log \overline{\mathrm{BHAR}}$–$\log \Sigma_1$ relation does not exhibit significant changes with redshift, $\overline{\mathrm{BHAR}}$ at a given Σ_1 evolves with redshift in a manner that could be well explained by the cosmic evolution of the gas content (Sections 3.3 and 4.1). The $\overline{\mathrm{BHAR}}$–Σ_1 relation among SF galaxies could suggest a link between BH growth and the central (∼kpc scale) gas density of host galaxies. A common origin for gas in the vicinity of the BH and in the central ∼kpc part of the galaxy may be further implied by this relation. The $\overline{\mathrm{BHAR}}$–Σ_1 relation could also be interpreted as a relation between BH growth and the central velocity dispersion of host galaxies at a given gas content, indicating the role of the host-galaxy potential well in feeding BHs (Section 4.1).

(iv) The quantitatively derived $\overline{\mathrm{BHAR}}$–Σ_1 relation in Section 3.3 has the potential to explain local BH 'monsters' among compact galaxies (Section 4.2). It is plausible that both the $\overline{\mathrm{BHAR}}$–Σ_1 and M_{BH}–M_{bulge} relations manifest the same underlying link between BH growth and host galaxies discussed in Section 4.1, and local BH 'monsters' deviate from the M_{BH}–M_{bulge} relation simply because the total SFR of ultracompact bulges cannot approximate the central ∼kpc gas density (or the velocity dispersion) well.

In the future, deep *James Webb Space Telescope* (*JWST*) imaging combined with deep X-ray coverage could help to quantify the $\overline{\mathrm{BHAR}}$–Σ_1 relation among SF galaxies better with a larger sample of galaxies/AGNs that has lower limiting $M_\star$. *JWST* integral field unit (IFU) observations (as well as grism observations) could measure the gas/stellar velocity dispersion of galaxies/AGNs, enabling the first characterization of the $\overline{\mathrm{BHAR}}$–σ relation. Future accumulation of ALMA pointings that have *HST*-like resolution in deep X-ray survey fields could help to probe the relation between BH growth and host-galaxy central gas density directly. Quantifying these relations could provide insights into the feeding mechanism of BHs, and how it links with the host galaxies.

ACKNOWLEDGEMENTS

We thank the anonymous referee for helpful feedback. We thank Robin Ciardullo and Marc Huertas-Company for helpful discussions. QN and WNB acknowledge support from *Chandra* X-ray Center grant GO8-19076X, NASA grant 80NSSC19K0961, and the V. M. Willaman Endowment. BL acknowledges financial support from the NSFC grants 11991053 and 11673010 and National Key Research and Development Program of China grant 2016YFA0400702. YQX acknowledges support from NSFC-11890693, NSFC-11421303, the CAS Frontier Science Key Research Program (QYZDJ-SSW-SLH006), and K. C. Wong Education Foundation.

DATA AVAILABILITY

The data underlying this paper were accessed from the NASA/IPAC Infrared Science Archive (IRSA) COSMOS data base (https://irsa.ipac.caltech.edu/Missions/cosmos.html). The derived data generated in this research will be shared on reasonable request to the corresponding author.

REFERENCES

Abramowicz M. A., Fragile P. C., 2013, Living Rev. Relativ., 16, 1
Aird J., Coil A. L., Georgakakis A., 2017, MNRAS, 465, 3390
Aird J., Coil A. L., Georgakakis A., 2018, MNRAS, 474, 1225
Barden M., Häußler B., Peng C. Y., McIntosh D. H., Guo Y., 2012, MNRAS, 422, 449
Barro G. et al., 2017, ApJ, 840, 47
Bertin E., Arnouts S., 1996, A&AS, 117, 393
Bezanson R. et al., 2011, ApJ, 737, L31
Bondi H., 1952, MNRAS, 112, 195
Boquien M., Burgarella D., Roehlly Y., Buat V., Ciesla L., Corre D., Inoue A. K., Salas H., 2019, A&A, 622, A103
Brandt W. N., Alexander D. M., 2015, A&AR, 23, 1
Buchner J., Bauer F. E., 2017, MNRAS, 465, 4348
Calzetti D., Armus L., Bohlin R. C., Kinney A. L., Koornneef J., Storchi-Bergmann T., 2000, ApJ, 533, 682
Cano-Díaz M. et al., 2016, ApJ, 821, L26
Capak P. et al., 2007, ApJS, 172, 99
Chabrier G., 2003, PASP, 115, 763
Chen C.-T. J. et al., 2013, ApJ, 773, 3
Chollet F. et al., 2015, Keras. Available at: https://github.com/fchollet/keras
Ciesla L. et al., 2015, A&A, 576, A10
Civano F. et al., 2016, ApJ, 819, 62
Dale D. A., Helou G., Magdis G. E., Armus L., Díaz-Santos T., Shi Y., 2014, ApJ, 784, 83
D'Amato Q. et al., 2020, A&A, 636, A37
Dekel A., Lapiner S., Dubois Y., 2019, preprint (arXiv:1904.08431)
De Lucia G., Springel V., White S. D. M., Croton D., Kauffmann G., 2006, MNRAS, 366, 499
Delvecchio I. et al., 2017, A&A, 602, A3
Ding X. et al., 2020, ApJ, 888, 37
Fang J. J., Faber S. M., Koo D. C., Dekel A., 2013, ApJ, 776, 63
Foreman-Mackey D., Hogg D. W., Lang D., Goodman J., 2013, PASP, 125, 306
Fragos T., Lehmer B. D., Naoz S., Zezas A., Basu-Zych A., 2013, ApJ, 776, L31
Gabor J. M. et al., 2009, ApJ, 691, 705
Graham A. W., Durré M., Savorgnan G. A. D., Medling A. M., Batcheldor D., Scott N., Watson B., Marconi A., 2016, ApJ, 819, 43
Grogin N. A. et al., 2011, ApJS, 197, 35
Habouzit M. et al., 2019, MNRAS, 484, 4413
Hani M. H., Hayward C. C., Orr M. E., Ellison S. L., Torrey P., Murray N., Wetzel A., Faucher-Giguère C.-A., 2020, MNRAS, 493, L87
Hasinger G. et al., 2018, ApJ, 858, 77
Häussler B. et al., 2007, ApJS, 172, 615
Hickox R. C., Mullaney J. R., Alexander D. M., Chen C.-T. J., Civano F. M., Goulding A. D., Hainline K. N., 2014, ApJ, 782, 9
Hodge J. A., da Cunha E., 2020, preprint (arXiv:2004.00934)
Hopkins P. F., Richards G. T., Hernquist L., 2007, ApJ, 654, 731
Hsieh B. C. et al., 2017, ApJ, 851, L24
Huertas-Company M. et al., 2015, ApJS, 221, 8
Ilbert O. et al., 2013, A&A, 556, A55
Jin S. et al., 2018, ApJ, 864, 56
Just D. W., Brandt W. N., Shemmer O., Steffen A. T., Schneider D. P., Chartas G., Garmire G. P., 2007, ApJ, 665, 1004
Kartaltepe J. S. et al., 2015, ApJS, 221, 11
Kennicutt Robert C. J., 1998a, ARA&A, 36, 189
Kennicutt Robert C. J., 1998b, ApJ, 498, 541

Kim S., 2015, Commun. Stat. Applications Methods, 22, 665
King A., 2005, ApJ, 635, L121
King A. R., 2010, MNRAS, 402, 1516
Kingma D. P., Ba J., 2014, preprint (arXiv:1412.6980)
Kirkpatrick A. et al., 2012, ApJ, 759, 139
Kocevski D. D. et al., 2017, ApJ, 846, 112
Koekemoer A. M. et al., 2007, ApJS, 172, 196
Koekemoer A. M. et al., 2011, ApJS, 197, 36
Kormendy J., Ho L. C., 2013, ARA&A, 51, 511
Kormendy J., Fisher D. B., Cornell M. E., Bender R., 2009, ApJS, 182, 216
Krist J., 1995, in Shaw R. A., Payne H. E., Hayes J. J. E., eds, ASP Conf. Ser. Vol. 77, Astronomical Data Analysis Software and Systems IV. Astron. Soc. Pac., San Francisco, p. 349
Laigle C. et al., 2016, ApJS, 224, 24
Leauthaud A. et al., 2007, ApJS, 172, 219
Lehmer B. D. et al., 2016, ApJ, 825, 7
Leja J. et al., 2019, ApJ, 877, 140
Leja J., Speagle J. S., Johnson B. D., Conroy C., van Dokkum P., Franx M., 2020, ApJ, 893, 111
Lin L. et al., 2019, ApJ, 884, L33
Liu D. et al., 2018, ApJ, 853, 172
Lutz D. et al., 2011, A&A, 532, A90
McConnell N. J., Ma C.-P., 2013, ApJ, 764, 184
Magorrian J. et al., 1998, AJ, 115, 2285
Marchesi S. et al., 2016a, ApJ, 817, 34
Marchesi S. et al., 2016b, ApJ, 830, 100
Marconi A., Hunt L. K., 2003, ApJ, 589, L21
Matharu J. et al., 2019, MNRAS, 484, 595
Mullaney J. R. et al., 2012, ApJ, 753, L30
Murray N., Quataert E., Thompson T. A., 2005, ApJ, 618, 569
Nair V., Hinton G. E., 2010, in Fürnkranz J., Joachims T., eds, Proceedings of the 27th international Conference on Machine Learning (ICML-10). Omnipress, Madison, WI, p. 807
Nelson E. J. et al., 2012, ApJ, 747, L28
Netzer H., 2015, ARA&A, 53, 365
Ni Q., Yang G., Brandt W. N., Alexander D. M., Chen C. T. J., Luo B., Vito F., Xue Y. Q., 2019, MNRAS, 490, 1135
Oliver S. J. et al., 2012, MNRAS, 424, 1614
Peng C. Y., Ho L. C., Impey C. D., Rix H.-W., 2002, AJ, 124, 266
Reines A. E., Volonteri M., 2015, ApJ, 813, 82
Rhodes J. D., Massey R., Albert J., Taylor J. E., Koekemoer A. M., Leauthaud A., 2006, in Koekemoer A. M., Goudfrooij P., Dressel L. L., eds, The 2005 HST Calibration Workshop: Hubble After the Transition to Two-Gyro Mode. NASA Goddard Space Flight Center, Greenbelt, MD, p. 21
Rhodes J. D. et al., 2007, ApJS, 172, 203
Sargent M. T. et al., 2007, ApJS, 172, 434
Sartori L. F., Schawinski K., Trakhtenbrot B., Caplar N., Treister E., Koss M. J., Urry C. M., Zhang C. E., 2018, MNRAS, 476, L34
Scarlata C. et al., 2007, ApJS, 172, 406
Schinnerer E. et al., 2016, ApJ, 833, 112
Shankar F. et al., 2020, MNRAS, 493, 1500
Silk J., Rees M. J., 1998, A&A, 331, L1
Springel V., Di Matteo T., Hernquist L., 2005, MNRAS, 361, 776
Stalevski M., Fritz J., Baes M., Nakos T., Popović L. Č., 2012, MNRAS, 420, 2756
Stalevski M., Ricci C., Ueda Y., Lira P., Fritz J., Baes M., 2016, MNRAS, 458, 2288
Storchi-Bergmann T., Schnorr-Müller A., 2019, Nat. Astron., 3, 48
Suh H., Civano F., Trakhtenbrot B., Shankar F., Hasinger G., Sanders D. B., Allevato V., 2020, ApJ, 889, 32
Sun M. et al., 2015, ApJ, 802, 14
Tacconi L. J. et al., 2018, ApJ, 853, 179
Taylor E. N., Franx M., Brinchmann J., van der Wel A., van Dokkum P. G., 2010, ApJ, 722, 1
Thomas D., Maraston C., Bender R., Mendes de Oliveira C., 2005, ApJ, 621, 673
Thomas D., Maraston C., Schawinski K., Sarzi M., Silk J., 2010, MNRAS, 404, 1775
Trayford J. W., Schaye J., 2019, MNRAS, 485, 5715
van der Wel A. et al., 2012, ApJS, 203, 24
Walsh J. L., van den Bosch R. C. E., Gebhardt K., Yildirim A., Gültekin K., Husemann B., Richstone D. O., 2015, ApJ, 808, 183
Walsh J. L., van den Bosch R. C. E., Gebhardt K., Yıldırım A., Gültekin K., Husemann B., Richstone D. O., 2017, ApJ, 835, 208
Wellons S. et al., 2015, MNRAS, 449, 361
Whitaker K. E., van Dokkum P. G., Brammer G., Franx M., 2012, ApJ, 754, L29
Whitaker K. E. et al., 2017, ApJ, 838, 19
Wuyts S. et al., 2011, ApJ, 738, 106
Yang G. et al., 2016, ApJ, 831, 145
Yang G. et al., 2017, ApJ, 842, 72
Yang G. et al., 2018a, MNRAS, 475, 1887
Yang G., Brandt W. N., Darvish B., Chen C. T. J., Vito F., Alexander D. M., Bauer F. E., Trump J. R., 2018b, MNRAS, 480, 1022
Yang G., Brandt W. N., Alexander D. M., Chen C. T. J., Ni Q., Vito F., Zhu F. F., 2019, MNRAS, 485, 3721
Yang G. et al., 2020, MNRAS, 491, 740
Yuan F., Narayan R., 2014, ARA&A, 52, 529
Yuan F., Yoon D., Li Y.-P., Gan Z.-M., Ho L. C., Guo F., 2018, ApJ, 857, 121
Zubovas K., King A., 2019, MNRAS, 484, 1829

APPENDIX A: ASSESSING $M_\star$ AND SFR MEASUREMENTS FROM X-CIGALE

In Table A1, we list the parameters used to construct the SED templates when fitting $M_\star$ and SFR with X-CIGALE in Section 2.1. In Fig. A1, we show the comparison between our SED-based $M_\star$ (SFR) measurements with X-CIGALE and SED-based $M_\star$ (SFR) measurements with PROSPECTOR in Leja et al. (2020) for $\log M_\star > 9.5$ COSMOS SF galaxies at $z = 0.2$–0.8, as well as the comparison of the obtained specific SFR (sSFR; which is calculated as SFR/$M_\star$). In Leja et al. (2020), a more flexible non-parametric SFH, a more flexible dust attenuation law, and a more flexible dust-emission model are utilized, which is beyond the scope of this work due to the large amount of computational time needed. We can see that our $M_\star$ measurements are systemically smaller than those reported in Leja et al. (2020) by ≈0.15 dex. As reported in Leja et al. (2019), this offset is expected mainly due to the usage of a non-parametric SFH in PROSPECTOR. We correct for this systematic offset in the final adopted $M_\star$ values (by adding 0.15 dex to the obtained $\log M_\star$ values), though we note that as we only quantitatively study the slope of the $\log \overline{\mathrm{BHAR}}$–$\log \Sigma_1$ relation in this paper, the systematic offset in $M_\star$ measurements should not affect our results. Our SFR measurements do not show any systematic offset when compared with SFR measurements in Leja et al. (2020). The relatively small scatter of ≈0.1 dex in $M_\star$ and ≈0.2 dex in SFR between the two sets of measurements demonstrates that though our adopted SED libraries may not be the ideal approach, they are acceptable for this analysis. We verified that our results in Section 3 are not materially affected if we add random perturbations to $\log M_\star$/log SFR with a scatter of 0.1/0.2 dex. For X-ray detected galaxies especially, the systematic offset and the scatter of $M_\star$ are close to those for the general galaxy population; there is a ≈0.1 dex offset between the two sets of SFR measurements (SFR values measured via X-CIGALE are systematically smaller than those measured via PROSPECTOR) and the scatter is relatively larger (≈0.35 dex) due to the default usage of AGN templates in our study (SED-based SFR measurements mainly depend on the UV and IR SED where the AGN component has non-negligible contributions). We note that even with the offset and the relatively larger scatter, ≈81 per cent of X-ray detected objects have SFR values in the two sets of measurements agreeing within 0.5 dex. Perturbing the log SFR values of X-ray detected galaxies in our

Table A1. Utilized X-CIGALE modules with fitting parameters. Default values are adopted for parameters not listed.

Module	Parameters	Values
Star formation history: *sfhdelayed*	τ (Myr)	100, 150, 200, 250, 300, 350, 400, 500, 600, 800, 1200, 2000, 3000, 5000, 8000
	t (Myr)	50, 100, 200, 300, 400, 500, 600, 800, 1000, 1500, 2000, 2500, 3000, 3500, 4000, 5000, 6000, 8000, 10 000
Stellar population synthesis model: *bc03*	Initial mass function	Chabrier (2003)
	Metallicity	0.02
Nebular emission: *nebular*	–	–
Dust attenuation: *dustatt_calzetti*	$E(B-V)$ for the young population	0.0–1.5 in a step of 0.1
	$E(B-V)$ reduction factor of the old population	0.44
Dust emission: *dale2014*	α in $\mathrm{d}M_{\mathrm{dust}} \propto U^{-\alpha}\mathrm{d}U$	1.5, 2.0, 2.5
AGN emission: *skirtor2016*	Torus optical depth at 9.7 μm	7
	Viewing angle (°)	30, 70
	AGN fraction in total IR luminosity ($\mathrm{frac}_{\mathrm{AGN}}$)	0–0.9 in a step of 0.1, 0.99
	$E(B-V)$ of AGN polar dust	0.1, 0.2, 0.3, 0.4, 0.5

sample by this large scatter also does not affect the analysis results in Section 3 materially.

We also compare our SED-based SFR measurements with FIR-based SFR measurements, as can be seen in Fig. A2. We can see that the median offset between the two measurements is small (≈0.19 dex; SFR values measured via X-CIGALE are systematically smaller than those measured from FIR luminosity). For ≈87 per cent of the objects (≈73 per cent of X-ray detected objects), SFR values measured by these two methods agree within 0.5 dex. This general agreement is sufficient in the context of this work, as we group sources into log SFR bins of at least ≈0.5 dex width in our analyses (see Section 3.2).

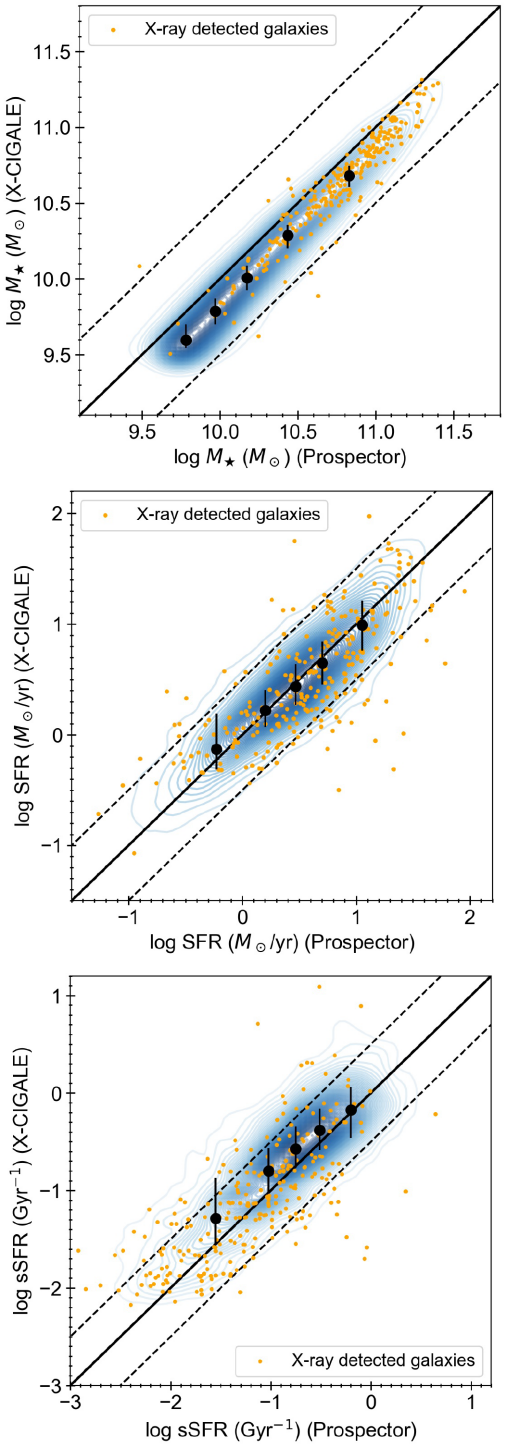

Figure A1. Upper panel: 2D KDE plot of $M_\star$ measured with X-CIGALE versus $M_\star$ measured in Leja et al. (2020) with PROSPECTOR in log–log space. The orange dots represent X-ray detected galaxies in our sample where an AGN component is added during the SED fitting. Black error bars represent the median X-CIGALE-based $M_\star$ value in different bins of $M_\star$ measured with PROSPECTOR and the scatter between the two sets of measurements in each bin. The black solid line represents a 1:1 relation; the black dashed lines represent 0.5 dex offsets from the 1:1 relation. Middle panel: similar to the upper panel, but for the two sets of SFR measurements. Lower panel: similar to the upper panel, but for the two sets of sSFR measurements.

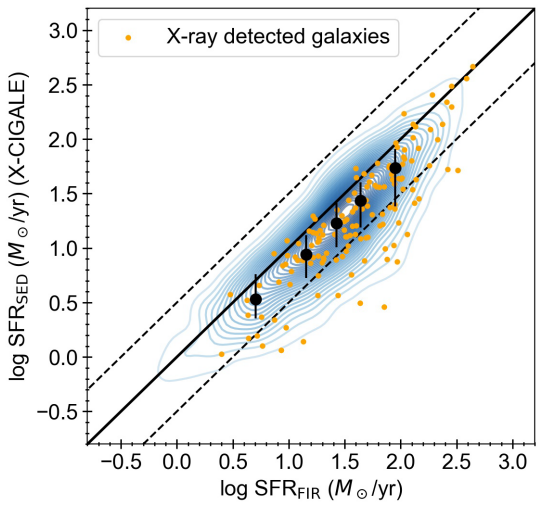

Figure A2. Similar to Fig. A1, but for SED-based SFR values (measured with X-CIGALE) versus FIR-based SFR values for all log $M_\star > 9.5$ COSMOS galaxies.

APPENDIX B: ASSESSING STRUCTURAL MEASUREMENTS FROM GALFIT

Sargent et al. (2007) provide GIM2D structural measurements for $I_{F814W} < 22.5$ objects in COSMOS. We compare our measured r_e values and n values with those reported in Sargent et al. (2007) in Fig. B1. As can be seen from the figure, our r_e and n measurements have negligible systematic offsets when compared with Sargent et al. (2007) (our r_e and n values are slightly larger in general), and the scatter between the two sets of measurements is ≈0.05 dex for r_e and ≈0.1 dex for n,[14] which demonstrates that our structural measurements are consistent with Sargent et al. (2007).

We note that while point-like emission from AGNs has the potential to contaminate host-galaxy light profiles that may affect the reliability of structural measurements, this contamination is small in our sample (where AGNs that dominate over host galaxies are removed; see Section 2.4). We stack the I_{814W}-band surface-brightness profiles of ≈650 X-ray AGNs (log $L_X > 42$ sources) at $z < 1.2$ in our compilation. For each of these X-ray AGNs, we select one galaxy not detected in the X-ray that has the closest n and r_e values to it (without duplications). We then stack the I_{814W}-band surface-brightness profiles of these matched X-ray undetected galaxies. The comparison between the stacked surface-brightness profiles of X-ray AGNs and X-ray undetected galaxies with similar structural parameters can be seen in Fig. B2. We can see that the stacked surface-brightness profile of X-ray AGNs is very similar to that of X-ray undetected galaxies. There is no obvious 'excess' in the centre that would suggest nuclear contamination from AGNs (see section 3.1 of Kocevski et al. 2017). The median reduced χ^2 of the single-component Sérsic fits of X-ray AGNs (≈1.1) is also similar to that of X-ray undetected galaxies. We model how the point-like emission from AGN may affect the host-galaxy surface-brightness profile: for the stacked surface-brightness profile of X-ray undetected galaxies, we add point-like emission that accounts for

[14] We note that the differences in r_e or n between the two sets of measurements do not have significant dependence on apparent magnitude.

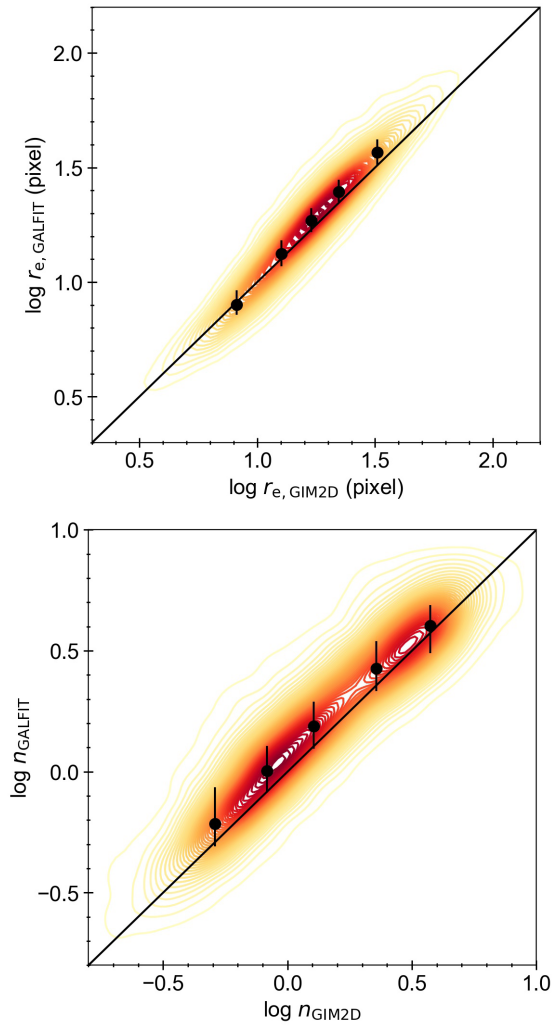

Figure B1. Upper panel: 2D KDE plot of our r_e values measured with GALFIT versus r_e measured with GIM2D (Sargent et al. 2007) in log–log space. Black error bars represent the median GALFIT-based r_e in different bins of GIM2D-based r_e and the scatter between the two sets of measurements in each bin. The black solid line represents a 1:1 relation. Lower panel: similar to the upper panel, but for n measured with GALFIT versus n measured with GIM2D in Sargent et al. (2007).

≈5 per cent of the total integrated light (the point-like emission is modelled utilizing the PSF generated in Section 2.2.2). Typically, when the PSF contamination is ≳5–10 per cent, GALFIT will hit the $r_e = 0.5$ and/or $n = 8$ constraint we set in Section 2.2 for the single-component Sérsic fitting, so that the object will not be utilized. For example, if we use GALFIT to fit the obtained composite light profile (the stacked light profile of matched X-ray undetected galaxies plus a 5 per cent PSF contamination; see the blue curve in Fig. B2), we hit the constraints mentioned above. In the centres of galaxies, the obtained composite surface-brightness profile clearly shows higher surface brightness than that of X-ray AGNs (see Fig. B2). Thus, the contamination to the host-galaxy light profile in the *HST* F814W band is small for X-ray AGNs in our sample.[15] For comparison, we also show the

[15]We note that it is unlikely for a galaxy to mimic the light profile of a galaxy with much more concentrated Sérsic profile when there is a moderate level of AGN contamination (≲5–10 per cent), so that this mode of contamination has limited influence for the Σ_1 measurements. While ≈80 per cent of the light from a point-like source is concentrated within a radius of 5 pixels (0.15 arcsec) according to the COSMOS I_{814W}-band PSF model, a large fraction of the light from a low-to-moderate-redshift galaxy lies outside the central 5-pixel-radius region, and the Sérsic-profile fitting will likely be dominated by this part of the light. For the stacked I_{814W}-band light profile of galaxies that host X-ray AGNs shown in Fig. B2, ≈86 per cent of the light lies outside the central 5-pixel-radius region. Even for a BD galaxy with $r_e \approx 1$ kpc at $z = 1.2$, ≈50 per cent of the light lies outside the central 5-pixel-radius region.

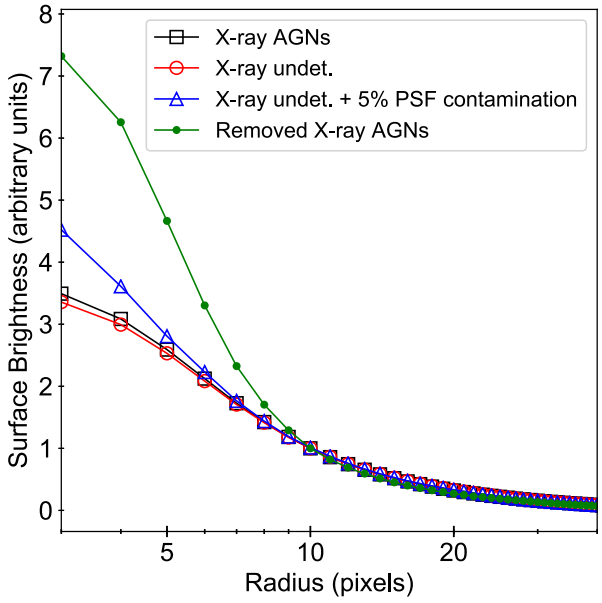

Figure B2. Stacked I_{814W}-band surface-brightness profiles of X-ray AGNs (black squares) and X-ray undetected galaxies with similar n and r_e values (red circles). The blue triangles show the modelled surface-brightness profile when X-ray undetected galaxies have a ≈5 per cent contamination to their total integrated light from AGNs on average. The green dots show the stacked surface-brightness profile of removed X-ray AGNs in Section 2.4.

stacked surface-brightness profile of X-ray AGNs removed from our sample in Fig. B2, which demonstrates high levels of AGN contamination.

APPENDIX C: IDENTIFYING BD GALAXIES IN THE COSMOS FIELD

We classify galaxies as BD/non-BD utilizing a convolutional neural network (CNN). This machine-learning-based approach has been widely adopted to perform morphological classification of galaxies. For example, Huertas-Company et al. (2015) utilized a CNN that was trained based on the visual classification in Kartaltepe et al. (2015) to perform morphological classification for $H < 24.5$ galaxies in all the CANDELS fields, and the generated catalogue has been adopted in Ni et al. (2019).

To train the CNN, we select ≈8000 galaxies among all $I_{F814W} < 24$ galaxies (MU_CLASS = 1; MU_CLASS is a star/galaxy classifier in the COSMOS ACS catalogue; Leauthaud et al. 2007) in the COSMOS *HST* field (Capak et al. 2007; Leauthaud et al. 2007), and manually assign each of them a binary label of BD (1) or non-BD (0). In order to make the selection of BD galaxies consistent with Kartaltepe et al. (2015) and Huertas-Company et al. (2015)

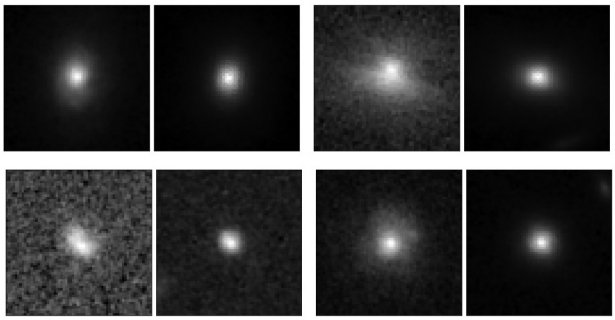

Figure C1. Examples of BD galaxies classified in Huertas-Company et al. (2015) with H_{160W}-band images, but not classified as BD galaxies in our training sample. In each subfigure, the left-hand panel is the I_{814W}-band cut-out of size 64 × 64 pixels, and the right-hand panel is the H_{160W}-band cut-out of size 64 × 64 pixels.

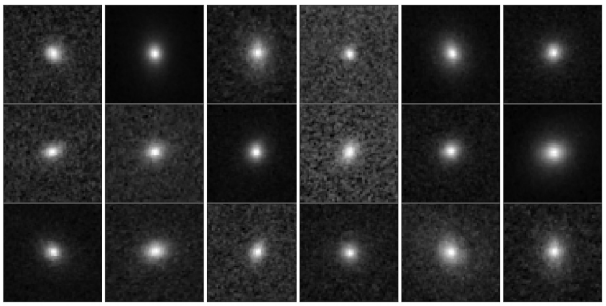

Figure C2. Example I_{814W}-band cut-outs (64 × 64 pixels) of BD galaxies visually identified in the training set.

(here we are pointing to objects with $f_{sph} > 2/3$, $f_{disc} < 2/3$, and $f_{irr} < 1/10$), 4015 galaxies in the training set are selected from the CANDELS–COSMOS field, where morphological classifications from Huertas-Company et al. (2015) are available. When labelling these sources, we try to be consistent with Huertas-Company et al. (2015), and the overall agreement is ≈95 per cent. Approximately 71 per cent/99 per cent of BD/non-BD galaxies identified in Huertas-Company et al. (2015) are still labelled as BD/non-BD galaxies. The reason for the relatively low level of agreement among BD galaxies can be attributed to both the morphological *k*-correction and the different angular resolution of CANDELS F160W images (0.06 arcsec pixel^{-1}) and COSMOS F814W images (0.03 arcsec pixel^{-1}) (see Fig. C1). The other 4271 galaxies are randomly selected across the whole COSMOS field, and we visually classify them as consistently as possible. Among the 8286 galaxies in total, 891 galaxies are classified as BD galaxies (see Fig. C2).

We split these labelled galaxies into a training set (5286 galaxies), a validation set (1500 galaxies), and a test set (1500 galaxies).[16] We then create cut-outs for them of size 64 × 64 pixels from ACS COSMOS science images v2.0 (Koekemoer et al. 2007), and store the normalized FITS file as NUMPY arrays.

Before the training, we copy the training set nine times and add random Gaussian noise (that is small enough so that the overall galaxy morphology/structure does not have noticeable changes),

[16]The relatively large number of objects placed in the validation/test set compared to common practice is due to the limited fraction (≈10 per cent) of BD galaxies: the number of BD galaxies in the validation/test set should be large enough for reasonable statistics.

Table C1. Convolutional neural network (CNN) configuration.

Layer	Filter size	Feature number	Output shape
Conv2D	3 × 3	32	(64, 64, 32)
Conv2D	3 × 3	32	(64, 64, 32)
MaxPooling2D	2 × 2	–	(32, 32, 32)
Conv2D	3 × 3	64	(32, 32, 64)
Conv2D	3 × 3	64	(32, 32, 64)
MaxPooling2D	2 × 2	–	(16, 16, 64)
Conv2D	3 × 3	128	(16, 16, 128)
Conv2D	3 × 3	128	(16, 16, 128)
MaxPooling2D	2 × 2	–	(8, 8, 128)
Dense	–	1024	1024
Dropout(0.2)	–	–	1024
Dense	–	1	1

which has proved to be a good approach for data augmentation (e.g. Huertas-Company et al. 2015). During the training, real-time random rotations, shifts in the centre position (less than 10 per cent of the total height and width), and zooms (between 75 per cent and 135 per cent) are also applied to the training set.

The CNN used in this work is implemented with the KERAS package (Chollet et al. 2015). The architecture of the CNN can be seen in Table C1. Hyperparameters including the network depth, filter size, and number of channels are optimized with the validation set. The activation function in between all the convolution and dense layers is Rectified Linear Unit (ReLU; e.g. Nair & Hinton 2010). A sigmoid function is applied to the last-layer output to compress it into [0, 1], which can be interpreted as the probability of being BD galaxies.

We use binary cross-entropy as the loss function, and we also apply the inverse class ratio as the weight to the loss to account for the sample imbalance. We use the Adam optimizer (Kingma & Ba 2014) to minimize the loss, and set the initial learning rate to be 0.0001. At the end of each learning epoch, we use the F_1 score to assess the model:

$$F_1 = \frac{2 \times \text{precision} \times \text{recall}}{\text{precision} + \text{recall}},$$

where

$$\text{precision} = \frac{\text{true positive (TP)}}{\text{true positive (TP)} + \text{false positive (FP)}},$$

$$\text{recall} = \frac{\text{true positive (TP)}}{\text{true positive (TP)} + \text{false negative (FN)}}.$$

The F_1 score is widely used to assess the quality of binary classification. For imbalanced data sets, it is more sensitive to the true quality of classification than accuracy. We drop the learning rate by a factor of 2 if the F_1 score of the validation set stops increasing for 10 epochs. When the F_1 score of the validation set stops increasing for 50 epochs, we stop the training process and save the model.

We test the obtained model with the test set. When converting the predicted probability into a binary label, we first use the default threshold of 0.5 to classify BD/non-BD galaxies, and we find that the number of FP is larger than the number of FN (due to the sample imbalance). For the purpose of this work, we require the 'contamination' in the BD sample to be as small as possible. Thus, we use the validation set to select a higher probability threshold that can make the number of FP approximately equal to the number of FN. The final training results can be seen in Table C2. We can correctly predict ≈87.3 per cent of BD galaxies and 98.4 per cent

Table C2. Training results assessed with the test set of 1500 galaxies.

TP	FP	TN	FN	Accuracy			F_1
				BD	Non-BD	Overall	
144	21	1314	21	87.3%	98.4%	97.2%	0.87

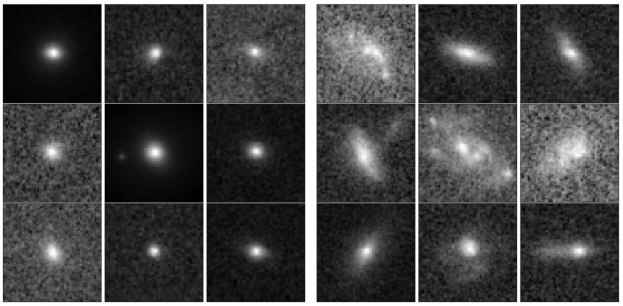

Figure C3. Example I_{814W}-band cut-outs (64 × 64 pixels) of deep-learning-predicted BD galaxies (left) and non-BD galaxies (right) in the COSMOS field.

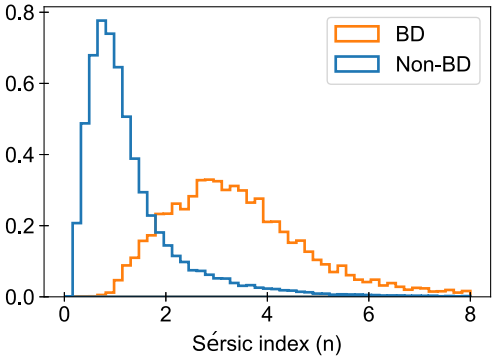

Figure C4. The Sérsic index distributions of the predicted BD galaxies and non-BD galaxies in the COSMOS field that demonstrate a clear distinction between the two populations.

of non-BD galaxies in the test set, and the number of predicted BD galaxies is roughly equal to the number of true BD galaxies.

With the trained CNN and the tuned probability threshold, we classify ≈115 000 $I_{F814W} < 24$ galaxies in the COSMOS ACS field as BD or non-BD. Fig. C3 shows example cut-outs of the predicted BD galaxies and non-BD galaxies (the presented galaxies are randomly drawn from the sample). In Fig. C4, we show the distributions of n among classified BD galaxies and non-BD galaxies. The clear separation in the distribution of n between the two populations demonstrates further the validity of our classification. We also note that our classification is consistent with that of Huertas-Company et al. (2015) when comparing the relative numbers of BD galaxies. At $z < 0.8$ and $\log M_\star > 10.2$, 2117 galaxies in our sample are classified as BD galaxies. This number is 453 for the CANDELS field, with BD galaxies identified in Huertas-Company et al. (2015). The ratio between these two numbers is roughly consistent with the ratio between our utilized area of COSMOS (≈1.4 deg^2) and the area of CANDELS (≈0.25 deg^2).

APPENDIX D: PCOR ANALYSES WITH DIFFERENT BINNING APPROACHES

We verified that the PCOR analysis results in Section 3 do not change qualitatively when the binning approach changes. Our finding in Section 3.1/Section 3.3 that the $\overline{\mathrm{BHAR}}$–Σ_1 relation is more fundamental than the $\overline{\mathrm{BHAR}}$–$M_\star$ relation for the SF non-BD/ALL SF sample holds true when we use 5 × 5 bins or 6 × 6 bins. Also, if we bin objects so that each 2D bin has the same number of X-ray detected galaxies (see Fig. D1), our results do not change qualitatively (see Table D1). Similarly, our finding in Section 3.2 that the $\overline{\mathrm{BHAR}}$–Σ_1 relation exists when controlling for SFR for the SF BD sample holds true when we use 4 × 4 bins; this result does not change qualitatively when we bin objects based on the number of X-ray detected galaxies (see the middle panel of Fig. D1 and Table D1).

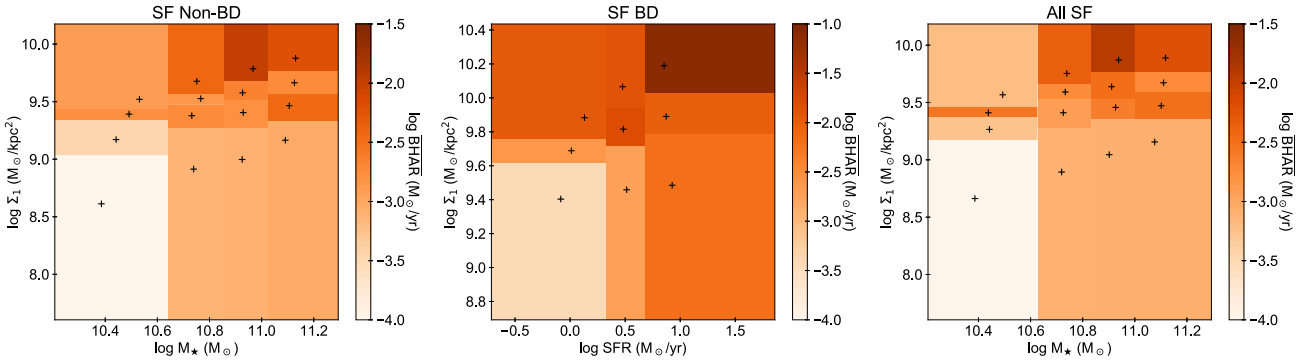

Figure D1. Left-hand panel: colour-coded $\overline{\mathrm{BHAR}}$ in different bins of $M_\star$ and Σ_1 for galaxies in the SF non-BD sample. Each 2D bin contains ≈11 X-ray detected galaxies. The black plus sign indicates the median $M_\star$ and Σ_1 of the sources in each bin. Middle panel: colour-coded $\overline{\mathrm{BHAR}}$ in different bins of SFR and Σ_1 for galaxies in the SF BD sample. Each 2D bin contains ≈9 X-ray detected galaxies. The black plus sign indicates the median SFR and Σ_1 of the sources in each bin. Right-hand panel: colour-coded $\overline{\mathrm{BHAR}}$ in different bins of $M_\star$ and Σ_1 for galaxies in the ALL SF sample. Each 2D bin contains ≈13 X-ray detected galaxies. The black plus sign indicates the median $M_\star$ and Σ_1 of the sources in each bin.

Table D1. *p*-values (significances) of PCOR analyses for the samples binned by the number of X-ray detected galaxies.

Relation	Pearson	Spearman
	SF non-BD	
$\overline{\mathrm{BHAR}}$–Σ_1	**9×10^{-5} (3.9σ)**	**2×10^{-4} (3.7σ)**
$\overline{\mathrm{BHAR}}$–$M_\star$	0.08 (1.8σ)	0.23 (1.2σ)
	SF BD	
$\overline{\mathrm{BHAR}}$–Σ_1	**2×10^{-3} (3.1σ)**	7×10^{-3} (2.7σ)
$\overline{\mathrm{BHAR}}$–SFR	0.04 (2.1σ)	0.73 (0.4σ)
	ALL SF	
$\overline{\mathrm{BHAR}}$–Σ_1	**2×10^{-4} (3.8σ)**	5×10^{-3} (2.8σ)
$\overline{\mathrm{BHAR}}$–$M_\star$	0.10 (1.6σ)	0.22 (1.2σ)

APPENDIX E: THE $\overline{\mathrm{BHAR}}$–SFR RELATION AMONG BD GALAXIES IN GENERAL

Though in Section 3.2 we found that among SF BD galaxies, the $\overline{\mathrm{BHAR}}$–Σ_1 relation is significant when controlling for SFR, while the $\overline{\mathrm{BHAR}}$–SFR relation is not significant when controlling for Σ_1, we note that the $\overline{\mathrm{BHAR}}$–SFR relation is still the dominant relation among BD galaxies in general (i.e. including quiescent BD galaxies; see Fig. E1), consistent with the findings in Yang et al. (2019). In Fig. E1, we show that the $\overline{\mathrm{BHAR}}$–SFR trend for all BD galaxies with $\log M_\star > 10$ at $z < 1.2$ in the COSMOS field is close to the $\overline{\mathrm{BHAR}}$–SFR relation obtained in Yang et al. (2019) utilizing $z = 0.5$–3 galaxies in the CANDELS field;[17] we also show that the difference in Σ_1 at a given SFR value does not associate with a significant difference in $\overline{\mathrm{BHAR}}$ except for the highest SFR bin (where a $\approx 3.7\sigma$ difference in $\overline{\mathrm{BHAR}}$ is associated with Σ_1).

As discussed in Ni et al. (2019) and in Section 4.2, the $\overline{\mathrm{BHAR}}$–SFR relation among BD galaxies and the $\overline{\mathrm{BHAR}}$–Σ_1 relation only among SF BD galaxies may reflect the same link between BH growth and the central ∼kpc gas density of host galaxies. When Σ_{gas} (or Σ_{SFR}) is roughly uniform across the bulge, the SFR among BD galaxiescould naturally serve as an indicator of the central ∼kpc gas density. Because of the compact sizes (on ∼kpc scale) of BD galaxies, even when the distribution of Σ_{gas} (or Σ_{SFR}) among a BD galaxy is far from uniform, we still expect a significant fraction of SFR to be enclosed in the central ∼kpc region. Thus, SFR could serve as an indicator of the central ∼kpc gas density among BD galaxies, though this relation suffers from a considerable scatter that originates from the scatter in the fraction of gas/SFR enclosed in the central ∼kpc region, similar to the uncertainty associated with the $\mathrm{SFR}_{\mathrm{bulge}}$–$\Sigma_{\mathrm{SFR,\,1\,kpc}}$ relation discussed in Footnote 13. Among SF BD galaxies, Σ_1 may serve as a better indicator of the central ∼kpc gas density (though this indicator only works for SF galaxies).

[17]The Yang et al. (2019) relation is well constrained from $\log \mathrm{SFR} \approx 1.5$ to $\log \mathrm{SFR} \approx -2$, probing $\log \overline{\mathrm{BHAR}}$ from ≈ -1 to ≈ -4.5, so that it could be applied to the parameter space probed in this work.

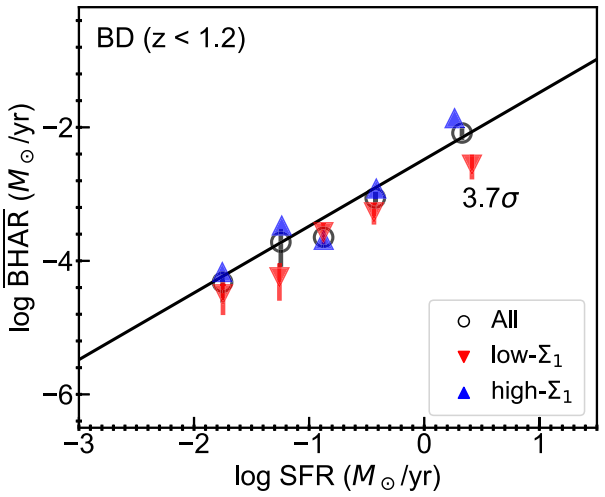

Figure E1. $\overline{\mathrm{BHAR}}$ versus SFR for BD galaxies with $\log M_\star > 10$ at $z < 1.2$ in the COSMOS field divided into SFR bins with ≈1000 sources per bin. Each SFR bin (black circles) is further divided into two subsamples with Σ_1 above (blue upward-pointing triangles) and below (red downward-pointing triangles) the median Σ_1 of the bin, respectively. The black solid line represents the best-fitting $\overline{\mathrm{BHAR}}$–SFR relation in Yang et al. (2019). We can see that the general $\overline{\mathrm{BHAR}}$–SFR trend is close to that obtained in Yang et al. (2019).

This paper has been typeset from a TEX/LATEX file prepared by the author.